The Effects of SST-Induced Surface Wind Speed and Direction Gradients on Midlatitude Surface Vorticity and Divergence

LARRY W. O'NEILL

Marine Meteorology Division, Naval Research Laboratory, Monterey, California

DUDLEY B. CHELTON

College of Oceanic and Atmospheric Sciences, and Cooperative Institute for Oceanographic Satellite Studies, Oregon State University, Corvallis, Oregon

STEVEN K. ESBENSEN

College of Oceanic and Atmospheric Sciences, Oregon State University, Corvallis, Oregon

(Manuscript received 2 May 2008, in final form 1 June 2009)

ABSTRACT

The effects of surface wind speed and direction gradients on midlatitude surface vorticity and divergence fields associated with mesoscale sea surface temperature (SST) variability having spatial scales of 100–1000 km are investigated using vector wind observations from the SeaWinds scatterometer on the Quick Scatterometer (QuikSCAT) satellite and SST from the Advanced Microwave Scanning Radiometer for Earth Observing System (AMSR-E) *Aqua* satellite. The wind–SST coupling is analyzed over the period June 2002–August 2008, corresponding to the first 6+ years of the AMSR-E mission. Previous studies have shown that strong wind speed gradients develop in response to persistent mesoscale SST features associated with the Kuroshio Extension, Gulf Stream, South Atlantic, and Agulhas Return Current regions. Midlatitude SST fronts also significantly modify surface wind direction; the surface wind speed and direction responses to typical SST differences of about 2°–4°C are, on average, about 1–2 m s^{-1} and 4°–8°, respectively, over all four regions. Wind speed perturbations are positively correlated and very nearly collocated spatially with the SST perturbations. Wind direction perturbations, however, are displaced meridionally from the SST perturbations, with cyclonic flow poleward of warm SST and anticyclonic flow poleward of cool SST.

Previous observational analyses have shown that small-scale perturbations in the surface vorticity and divergence fields are related linearly to the crosswind and downwind components of the SST gradient, respectively. When the vorticity and divergence fields are analyzed in curvilinear natural coordinates, the wind speed contributions to the SST-induced vorticity and divergence depend equally on the crosswind and downwind SST gradients, respectively. SST-induced wind direction gradients also significantly modify the vorticity and divergence fields, weakening the vorticity response to crosswind SST gradients while enhancing the divergence response to downwind SST gradients.

1. Introduction

On spatial scales spanning ocean basins, sea surface temperature (SST) perturbations are found to be negatively correlated with surface wind speed perturbations (e.g., Mantua et al. 1997; Okumura et al. 2001; Xie 2004). Over these broad spatial scales, large-scale atmospheric circulation patterns change surface ocean temperatures through modulation of surface heat fluxes and upper ocean mixing (e.g., Cayan 1992). On smaller spatial scales between 100 and 1000 km, however, surface wind speed and SST perturbations have a strong positive correlation in regions of large SST gradients, which occur near meandering ocean currents (see review by Small et al. 2008). Contemporaneous near-global satellite measurements of surface vector winds and SST have shown that these small-scale features in the surface wind field are particularly prevalent near large midlatitude ocean currents. Previous studies have only investigated

Corresponding author address: Larry W. O'Neill, Naval Research Laboratory, 7 Grace Hopper Ave., MS2, Monterey, CA 93943–5502.
E-mail: larry.oneill@nrlmry.navy.mil

DOI: 10.1175/2009JCLI2613.1

TABLE 1. Slopes of the linear relationships between the wind stress curl and crosswind SST gradient (α_C) and the wind stress divergence and downwind SST gradient (α_D) listed in previous studies over various regions in units of N m^{-2} per °C. Acronyms used here include: National Center for Atmospheric Research (NCAR) Community Climate System Model 3.0 (CCSM3.0); Model for Interdisciplinary Research on Climate 3.2 (MIROC3.2); Scripps Coupled Ocean–Atmosphere Regional (SCOAR) model; and Naval Research Laboratory Coupled Ocean–Atmosphere Mesoscale Prediction System (COAMPS) model. The ratio α_C/α_D is shown in the rightmost column.

Study	Region	Source	α_C	α_D	α_C/α_D
Chelton et al. (2001)	Tropical Pacific	QuikSCAT–TMI			
	3°N–1°S		0.0075	0.0135	0.56
	1°S–5°S		0.0112	0.0247	0.45
O'Neill et al. (2003)	Southern Ocean	QuikSCAT–Reynolds	0.0068	0.0124	0.55
Chelton et al. (2004)	Southern Ocean	QuikSCAT–AMSR	0.0117	0.0165	0.71
	Tropical Pacific		0.0084	0.0188	0.45
	Kuroshio		0.0057	0.0096	0.59
	Gulf Stream		0.0057	0.0109	0.52
Chelton (2005)	Tropical Pacific	QuikSCAT–TMI	0.0087	0.0145	0.60
			0.0080	0.0142	0.56
O'Neill et al. (2005)	Agulhas	QuikSCAT–AMSR	0.0213	0.0284	0.75
Maloney and Chelton (2006)	Agulhas	QuikSCAT–AMSR	0.0126	0.0173	0.73
		ECMWF	0.0041	0.0077	0.53
		NCAR CCSM3.0	0.0041	0.0088	0.47
		MIROC3.2	0.0074	0.0131	0.56
	Kuroshio	QuikSCAT–AMSR	0.0044	0.0070	0.63
		ECMWF	0.0016	0.0040	0.40
		NCAR CCSM3.0	0.0032	0.0065	0.49
		MIROC3.2	0.0021	0.0059	0.36
Seo et al. (2007)	Tropical Pacific	SCOAR	0.009	0.015	0.60
	Coastal California				
	36°–43°N		0.002	0.005	0.40
	32°–39°N		0.006	0.008	0.75
Chelton et al. (2007)	California current system	QuikSCAT–AMSR	0.0213	0.0301	0.71
Haack et al. (2008)	California current system	QuikSCAT COAMPS	0.0182	0.0260	0.70
			0.0157	0.0193	0.81

SST-induced changes in wind speed across SST fronts and not wind direction. The main objectives of this study are (i) to determine how small-scale SST perturbations affect both surface wind speed and direction from 6+ years of satellite observations of vector surface winds and SST and (ii) to determine their cumulative effects on the surface curl and divergence fields over the SST fronts associated with four midlatitude ocean currents: the Kuroshio Extension in the North Pacific, the Gulf Stream in the North Atlantic, the Brazil–Malvinas Confluence in the South Atlantic, and the Agulhas Return Current in the Indian Ocean sector of the Southern Ocean.

Spatial variations in surface wind speed associated with small-scale SST variability develop surface curl and divergence perturbations with magnitudes comparable to the large-scale curl and divergence (Chelton et al. 2004; O'Neill et al. 2003, 2005; Chelton et al. 2007). Satellite observations of these curl and divergence perturbations are remarkably well correlated with small-scale perturbations in the crosswind and downwind components of the SST gradient, respectively (Chelton et al. 2001, 2004, 2007; Chelton 2005; O'Neill et al. 2003, 2005). The surface wind stress curl and divergence fields are related linearly to the crosswind and downwind SST gradients, respectively. These curl and divergence dependencies are simulated to varying degrees in numerical weather predication and climate models (Maloney and Chelton 2006; Haack et al. 2008) and in regional mesoscale models (Seo et al. 2007; Spall 2007b).

In all past studies, the curl response to crosswind SST gradients has been found to be significantly weaker than the divergence response to downwind SST gradients, as measured by the slopes α_C and α_D, respectively, of the linear statistical relations (Table 1). The ratio of these slopes α_C/α_D varies between about 0.4 and 0.75. Additionally, satellite observations have shown strong seasonal variability in α_C and α_D (O'Neill et al. 2005; Maloney and Chelton 2006; O'Neill et al. 2009, manuscript submitted to *J. Climate*, hereafter OCE) and strong geographical variability between ocean basins (Chelton et al. 2004; OCE) and within individual regions (O'Neill et al. 2005). From a mesoscale modeling study over the Gulf Stream, Spall (2007b) noted that α_C has a significant quadratic dependence on the large-scale geostrophic wind speed. This is shown by OCE to result

from the nonlinearity between SST-induced surface wind speed and wind stress perturbations.

Beyond what is known about the dynamics of the near-surface wind response to small-scale SST perturbations, as discussed in section 2, little is known about the dynamics underlying the curl and divergence responses to SST gradients. The differences in the curl and divergence responses reveal an opportunity to better understand how the marine atmospheric boundary layer (MABL) responds to small-scale SST perturbations.

In this study, surface wind speed and direction are obtained from the SeaWinds scatterometer onboard the Quick Scatterometer (QuikSCAT) satellite and SST is obtained from the Advanced Microwave Scanning Radiometer for Earth Observing System (EOS) (AMSR-E) *Aqua* satellite, as discussed in section 3. The statistical responses of spatially high-pass filtered surface wind speed and direction as functions of SST are shown in section 4. A relatively simple statistical relation is found between surface wind speed and SST despite the complicated force balances involved in the SST-induced MABL response described by previous studies. In section 5, the QuikSCAT vorticity and divergence of the surface wind field are shown to depend on the crosswind and downwind SST gradients in a manner analogous to the dependencies of the wind stress curl and divergence considered in our previous studies. While the vorticity and divergence responses to SST gradients have been interpreted previously in terms of SST effects on surface wind stress magnitude (or wind speed), we show that SST also modifies the surface wind direction, thus also contributing to SST-induced changes in the surface vorticity and divergence. These SST-induced modifications of wind direction are shown to be responsible for the differing vorticity and divergence responses to SST. We close in section 6 with a discussion of the implications of the results of this study for coupled mesoscale wind–SST interactions.

2. Dynamical explanations for mesoscale wind–SST coupling

Many observational and modeling studies have now been undertaken to better understand the MABL response to SST perturbations over various regions of the World Ocean. The response of surface winds to mesoscale SST perturbations is the culmination of adjustment processes extending throughout the depth of the MABL and appears to be controlled mainly by modification of the surface heat fluxes as air flows across SST fronts. Surface heat fluxes are enhanced or suppressed depending on whether the flow is from cold to warm water or vice versa. Cross-frontal surface heating perturbations produce changes in the MABL hydrostatic pressure gradients and to the vertical turbulent stress divergence in the MABL as described below, ultimately leading to changes in near-surface winds coupled to the mesoscale SST perturbations.

Across SST fronts, variations in surface heating cause cross-frontal pressure gradients near the surface since a cooler MABL over cooler water forms higher surface pressures relative to a warmer MABL over warmer water. Thermally induced pressure gradients so formed can therefore accelerate near-surface flow across SST isotherms from cooler to warmer water and vice versa. Using an analytical model of the boundary layer, Lindzen and Nigam (1987) attributed acceleration of cross-equatorial surface flow north of the equatorial cold tongue in the eastern tropical Pacific primarily to thermally induced pressure gradients associated with the cold tongue meridional SST gradient. Even though some of the assumptions of their analytical model are not generally valid (e.g., Battisti et al. 1999; Stevens et al. 2002; Small et al. 2003), SST-induced pressure gradients are indeed strong contributors to the SST-induced surface wind response (e.g., Wai and Stage 1989; Warner et al. 1990; Small et al. 2003; Cronin et al. 2003; Mahrt et al. 2004; Bourras et al. 2004; Song et al. 2004; Small et al. 2005b; Song et al. 2006). Using mesoscale numerical simulations over the equatorial Pacific, Small et al. (2003) showed that near-surface pressure perturbations form in response to SST-induced MABL air temperature variations, which are governed thermodynamically by a balance between horizontal temperature advection and surface sensible heat fluxes. From surface pressure observations over the equatorial Pacific, Cronin et al. (2003) have shown that SST-induced surface pressure gradient perturbations associated with the northern equatorial cold tongue are of a magnitude similar to those generated by mesoscale model simulations. Hashizume et al. (2002) have also suggested that deepening and shoaling of the MABL associated with cross-frontal turbulent mixing variations counteracts this thermodynamic contribution to the SST-induced surface pressure variations in what has been referred to as a ''backpressure'' effect. Finally, while MABL pressure gradients contribute to near-surface flow acceleration perpendicular to SST isotherms, it is not clear how they contribute to the generation of near-surface vorticity as air blows parallel to SST isotherms, a feature generally observed in scatterometer wind fields globally.

Wallace et al. (1989) and Hayes et al. (1989) argued that vertical turbulent mixing of momentum from aloft to the surface was more consistent with the changes in vertical wind shear and the acceleration of surface winds occurring across the northern edge of the equatorial

Pacific cold tongue than with thermally induced pressure gradients. Earlier aircraft observations over the north wall of the Gulf Stream by Sweet et al. (1981) also showed that turbulent mixing of momentum from aloft to the surface also played a significant role in near-surface wind speed variations. With this mechanism, SST-induced surface heating modifies the static stability of the boundary layer, enhancing the vertical turbulent mixing of momentum as air blows from cool to warm water and reducing it as air blows from warm to cool water. Observations of the near-surface vertical turbulent momentum flux throughout the world's oceans have generally shown considerable variation upon crossing SST fronts and have supported this hypothesis (Mey and Walker 1990; Freihe et al. 1991; Bond 1992; Jury 1994; Rouault and Lutjeharms 2000; Mahrt et al. 2004; de Szoeke et al. 2005; Tokinaga et al. 2006).

Modeling studies of the surface wind response to mesoscale SST perturbations have been less consistent about the role that the vertical turbulent stress divergence plays in the SST-induced surface wind response. Some investigators find a significant role (Wai and Stage 1989; de Szoeke and Bretherton 2004; Bourras et al. 2004; Song et al. 2004; Skyllingstad et al. 2006; Thum 2006; Song et al. 2009; O'Neill et al. 2010) while others found less significant roles (Small et al. 2003; Bourras et al. 2004; Small et al. 2005a,b; Song et al. 2006; Samelson et al. 2006; Spall 2007b). Additionally, the contribution of surface ocean currents to the surface stress may play a small but nonnegligible role in the near-surface vertical turbulent stress divergence (Song et al. 2006; Liu et al. 2007). Idealized large-eddy simulations of the flow across sharp SST fronts by Skyllingstad et al. (2006) showed that on spatial scales of 1–20 km, which are somewhat smaller than considered here, near-surface wind speed variations are influenced predominantly by SST-induced cross-frontal variations in the vertical turbulent mixing of momentum, consistent with the Wallace et al. (1989) and Hayes et al. (1989) hypotheses. Finally, weak coupling of surface winds to SST in the European Centre for Medium-Range Weather Forecasts (ECMWF) model over the Agulhas Return Current (Maloney and Chelton 2006) was shown by Song et al. (2009) to be attributable primarily to a weak response of the parameterized vertical turbulent stress divergence to SST-induced surface heating perturbations.

Small et al. (2005a) envisioned a quite different role of the vertical turbulent stress divergence in a numerical simulation of the near-surface wind response over the eastern tropical Pacific. There, it was found that pressure gradients accelerated the near-surface flow across the cold tongue SST front, and after some distance, the vertical turbulent stress divergence acted as a frictional drag on this pressure-driven flow. In this ''pressure-drag'' mechanism, turbulence acts to reduce the surface winds in an opposite manner to that hypothesized by Wallace et al. (1989) and Hayes et al. (1989). This pressure-drag mechanism was found to operate in a numerical simulation over the Agulhas Return Current (O'Neill et al. 2010), but only above about 150 m from the surface; below this level, the near-surface winds were influenced by the turbulent mixing of momentum in accordance with the Wallace et al. (1989) and Hayes et al. (1989) mechanism.

Samelson et al. (2006) argued that changes in boundary layer depth somewhat downwind of the sharpest SST gradients, rather than the vertical redistribution of momentum, could act to change the surface stress. This mechanism acts through a balance of a fixed large-scale pressure gradient and the vertical turbulent stress divergence integrated vertically over the depth of the boundary layer such that the ratio of surface stress to boundary layer height τ/H is equal to a fixed large-scale pressure gradient integrated over the depth of the boundary layer. This balance was found to be consistent with the cross-frontal changes in surface stress and boundary layer height away from the steepest SST gradients in the two-dimensional model simulation of Spall (2007b). This balance assumes that the SST-induced responses of the vertical turbulent mixing of momentum, thermally induced pressure gradients, and horizontal advection are not significant terms in the MABL momentum budget in regions directly over the sharpest SST fronts (see detailed discussion in Small et al. 2008).

At midlatitudes, Coriolis accelerations have been shown to be important to the response of the surface winds to small-scale SST perturbations (e.g., Wai and Stage 1989; Bourras et al. 2004; Thum 2006; Song et al. 2006; Spall 2007b; O'Neill et al. 2010). Over a single SST front, Spall (2007b) has found that SST-induced turbulent mixing perturbations induce Coriolis accelerations analogous to an inertially driven lee wave. O'Neill et al. (2010) has found evidence of a similar mechanism in a simulation over a part of the Southern Ocean. The strong large-scale mean wind speeds typically found over midlatitude ocean fronts also lead to significant horizontal advective accelerations that strongly influence the near-surface momentum budget (Song et al. 2006; Thum 2006; Spall 2007b; O'Neill et al. 2010).

Some debate remains as to the physical mechanisms involved in the coupling between surface winds and mesoscale SST perturbations. It is becoming clear, however, that both pressure gradients and the turbulent mixing of momentum are involved significantly in the response. There are also likely significant regional differences in the large-scale atmospheric forcing that may alter the force balance involved in the surface wind

response. We show below that there are comparatively simple statistical relationships between the surface winds and SST despite the rather complicated details of these physical mechanisms.

3. Description of satellite observations and methods

This study utilizes monthly-averaged surface vector wind observations from the QuikSCAT scatterometer and SST from the AMSR-E over the 75-month period June 2002–August 2008, coinciding with the first 6+ years of the AMSR-E geophysical observational data record that began 1 June 2002. Each of these datasets is summarized in this section.

a. QuikSCAT wind fields

In nonprecipitating conditions, scatterometers infer surface vector winds over water from microwave radar measurements of small-scale surface roughness caused by surface wind stress. For lack of abundant direct surface stress measurements, scatterometer measurements of microwave radar backscatter are calibrated to buoy anemometer measurements of the so-called equivalent neutral stability wind at 10 m, which is the 10-m wind that would be uniquely related to the observed surface wind stress if the atmosphere were neutrally stratified (Liu and Tang 1996). The relation between the equivalent neutral stability wind vector $\mathbf{u}$ and the surface wind stress vector $\boldsymbol{\tau}$ is $\boldsymbol{\tau} = \rho_0 C_D^N V \mathbf{u}$, where ρ_0 is the surface air density, V is the magnitude of $\mathbf{u}$, and C_D^N is the neutral stability drag coefficient.

The computations throughout this paper using QuikSCAT winds are based on 10-m equivalent neutral stability winds. On average, anemometer measurements of the 10-m wind speed are about 0.2 m s^{-1} lower than the corresponding neutral-stability wind speed at 10 m (Mears et al. 2001; see also Fig. 16 of Chelton and Freilich 2005) because the atmospheric surface layer is, on average, slightly unstable over all oceans. Through comparisons with high-quality buoy anemometer measurements, QuikSCAT wind speed measurement errors have been estimated to be about 1.7 m s^{-1} (Chelton and Freilich 2005). The wind direction accuracy improves with increasing wind speed; for wind speeds greater than about 5 m s^{-1}, the direction accuracy of individual wind measurements is better than 15° (see Fig. 8 in Chelton and Freilich 2005). Additionally, there is no evidence of SST-dependent measurement biases in the QuikSCAT wind observations (Chelton et al. 2001; Ebuchi et al. 2002).

The spatial derivatives of wind components, wind speed, and wind direction analyzed in this study were computed "in-swath" before interpolating to a regular spatial grid. This avoids complications arising from the estimation of spatial derivatives near swath edges where centered first-difference estimates of derivatives are computed using measurements from neighboring swaths separated in time by several hours or more. The various wind and derivative wind fields of interest in this study were then constructed on a 0.25° latitude by 0.25° longitude spatial grid by fitting in-swath measurements to a quadratic surface using locally weighted regression ("loess" smoothing; Cleveland and Devlin 1988) with a half span of 80 km. Based on the filter transfer function of the loess smoother (Schlax et al. 2001; Chelton and Schlax 2003), the resulting gridded fields have a spatial resolution analogous to that of approximately 50-km block averages. The spatial derivative fields were found at each grid point directly from the regression coefficients of the quadratic surface. The wind fields were then averaged at monthly intervals from the gridded swath data.

b. AMSR-E SST fields

The detailed results of this study would not be possible without the near-all-weather microwave observations of SST over middle- and high-latitude regions provided by the AMSR-E since June 2002 (Chelton and Wentz 2005). The main advantage of microwave measurements of SST is the ability to measure SST through nonprecipitating clouds, which are essentially transparent to microwave radiation. Cloud cover generally obscures the midlatitude ocean regions of interest in this study more than 70% of the time (Chelton and Wentz 2005). Large regions of missing data often occur in SST fields constructed from infrared satellite measurements over the sharpest ocean fronts and eddies where strong ocean–atmosphere interactions are expected to occur (see, e.g., Fig. 6 of Chelton and Wentz 2005). Indeed, stratocumulus and cumulus cloud bands often form over sharp SST fronts as a consequence of some of the same MABL adjustment processes affecting MABL winds of interest in this study (e.g., Norris and Iacobellis 2005). While SST measurements by the Tropical Rainfall Measuring Mission (TRMM) Microwave Imager (TMI) have been available since December 1997 and thus encompass the entire QuikSCAT mission, they are only made equatorward of 40° latitude, leaving most of the midlatitude regions of interest in this analysis unsampled.

The AMSR-E measures horizontally and vertically polarized brightness temperatures at six microwave frequencies across a 1450-km swath. From these 12 microwave brightness temperatures, SST is estimated over most of the global oceans using a physically based statistical regression algorithm (Wentz and Meissner 2000). The footprint size of AMSR-E measurements of SST is 56 km and the rms accuracy of individual SST measurements is

about 0.4°C (Chelton and Wentz 2005). The SST fields were gridded onto the same 0.25° grid as the QuikSCAT surface wind fields and then averaged at monthly intervals.

c. Crosswind and downwind SST gradient computations

As discussed in the introduction, previous studies have shown that the wind stress curl and divergence fields are found to be related linearly to the crosswind and downwind components of the SST gradient, respectively. Crosswind and downwind gradients in this study were computed within each QuikSCAT measurement swath using curvilinear natural coordinates (s, n), where s and n are local along-wind and crosswind coordinates, respectively (e.g., Haltiner and Martin 1957; Holton 1992). The unit vector $\hat{\mathbf{s}}$ is in the same direction as $\mathbf{u}$. The positive unit vector $\hat{\mathbf{n}}$ points 90° counterclockwise relative to $\hat{\mathbf{s}}$. The crosswind and downwind components of the SST field $T(x, y)$ in natural coordinates are computed from Cartesian derivatives by

$$\frac{\partial T}{\partial n} = -\sin\psi\frac{\partial T}{\partial x} + \cos\psi\frac{\partial T}{\partial y} \quad \text{and}$$
$$\frac{\partial T}{\partial s} = \cos\psi\frac{\partial T}{\partial x} + \sin\psi\frac{\partial T}{\partial y}, \tag{1}$$

where (x, y) are the zonal and meridional Cartesian coordinates, respectively, and ψ is the counterclockwise surface wind direction relative to the x axis.

Crosswind and downwind SST gradients were computed here on a swath-by-swath basis by combining wind measurements from each QuikSCAT swath with SST gradients computed from gridded 3-day averaged AMSR-E SST fields centered on each day of the QuikSCAT measurement swath. Swaths of crosswind and downwind SST gradients were then averaged at monthly intervals. This procedure minimizes uncertainties associated with computing the nonlinear crosswind and downwind SST gradients from wind and SST measurements that are not collocated spatially and temporally.

d. Spatial high-pass filtering

SST-induced mesoscale wind variability was isolated by removing large-scale spatial variability using a multidimensional loess smoothing function with half-power filter cutoffs of 10° latitude × 20° longitude (Cleveland and Devlin 1988). This filtering effectively removes the large-scale components of the wind and SST fields that are unrelated to the wind–SST coupling of interest here. Wind and SST fields spatially high-pass filtered in this way are hereafter referred to as perturbation fields. To isolate the SST influence on surface winds that is of interest here, the effects of synoptic weather variability were mitigated by using monthly-averaged wind and SST fields. It is noted that this spatial filtering was applied on all variables after computations involving the wind and SST fields were performed, including the nonlinear crosswind and downwind gradient computations. This is preferable to computing the crosswind and downwind gradient quantities from monthly-averaged fields.[1]

4. Observations of SST-induced surface wind response

a. Surface wind speed response to SST

Maps of the QuikSCAT perturbation surface wind speed and the AMSR-E SST fields scalar-averaged over the 75-month analysis period are shown in Fig. 1 for each of the four regions considered here. Large horizontal variations in surface wind speed occur near meandering SST fronts, with stronger wind speeds over warmer water and weaker wind speeds over cooler water. Typically, surface wind speed variations of more than 1–2 m s^{-1} accompany SST variations of about 2°–4°C over cross-frontal distances of O(100 km). This is an appreciable fraction of the unfiltered scalar-averaged wind speeds in these regions (Fig. 2), which are typically 8–13 m s^{-1} in these long-term time averages. For the time-averaged perturbation fields, the spatial cross-correlation between the perturbation wind speed and the perturbation SST varies between 0.7 over the Kuroshio to 0.85 over the South Atlantic (Table 2). In addition to the quasi-stationary coupled patterns in the perturbation wind and SST fields apparent in these long-term time-averaged maps, there is also significant coupled variability associated with transient SST features evident from satellite data over the Kuroshio (e.g., Nonaka and Xie 2003), the Gulf Stream (e.g., Park and Cornillon 2002; Park et al. 2006), and all four midlatitude regions considered here (White and Annis 2003). The wind–SST coupling in the Kuroshio region is much more apparent during the boreal wintertime

[1] Crosswind and downwind gradients of SST in our previous studies (Chelton et al. 2001, 2004; O'Neill et al. 2003, 2005) were computed from gridded, vector-averaged wind stress and SST gradient components rather than being computed on a swath-by-swath basis and then averaging, which is more accurate because of the nonlinearity of these quantities. As a result, the SST-induced wind response in those studies was somewhat underestimated from those obtained from the more accurately computed quantities used here. Additionally, the definition of the crosswind SST gradient used in those studies $(\nabla T \times \hat{\mathbf{u}}) \cdot \hat{k}$ is equal to $-\partial T/\partial n$ and the downwind SST gradient $\nabla T \cdot \hat{\mathbf{u}}$ is equal to $\partial T/\partial s$, where $\hat{\mathbf{u}}$ is a unit vector in the direction of the surface wind vector and $\hat{k}$ is a unit vector in the vertical direction.

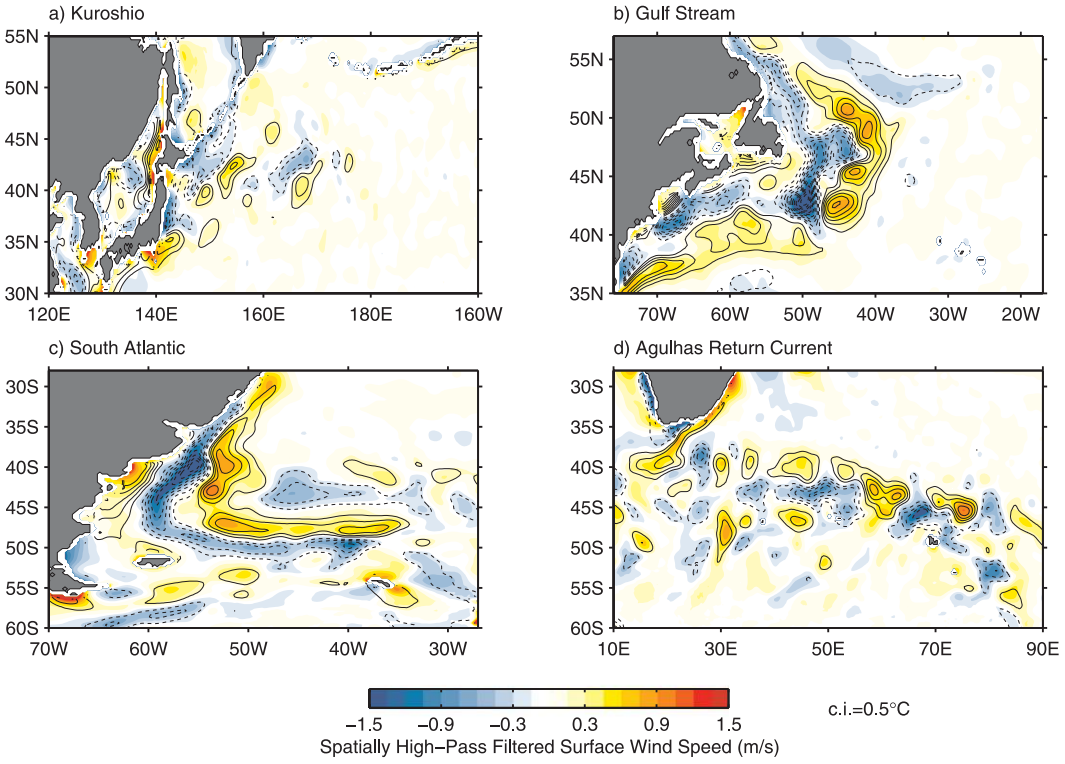

FIG. 1. Maps of the perturbation QuikSCAT wind speed (colors) and AMSR-E SST (contours) scalar-averaged over the period June 2002–August 2008 for the four regions considered in this study. The contour interval for the perturbation SST is 0.5°C, and the zero contour has been omitted for clarity. Solid and dashed contours correspond to positive and negative values, respectively. The spatial high-pass filter removes spatial variability with wavelengths longer than 20° longitude × 10° latitude, as discussed in the text.

(e.g., Nonaka and Xie 2003; OCE) and is associated with strong seasonality of the SST fronts in this region (e.g., Nonaka and Xie 2003).

The mesoscale response of the wind speed to SST is quantified statistically by bin-averaging monthly averages of the perturbation QuikSCAT wind speed as a function of the perturbation AMSR-E SST over the 75-month analysis period (Fig. 3). Wind speed perturbations are related linearly to, and correlated positively with, mesoscale SST perturbations over all four regions. The relationship between the monthly-averaged spatially high-pass filtered wind speed V' and SST T' can thus be expressed empirically as

$$V' = \alpha_v T', \tag{2}$$

where α_v is the least squares estimate of the slope of these linear relations and represents the change in wind speed per unit change in SST (i.e., $\alpha_v = \partial V'/\partial T'$) and the primes hereafter represent spatially high-pass filtered fields. Notably, α_v varies by nearly a factor of 2 geographically, from 0.27 m s^{-1} per °C over the Gulf Stream to 0.49 m s^{-1} per °C over the Agulhas Return Current (see Table 2). Additionally, α_v is much larger in the two Southern Hemisphere regions compared to those in the Northern Hemisphere. The larger error bars at large perturbation SST magnitudes in Fig. 3 are due to the smaller numbers of samples in these bins. This is particularly acute over the Kuroshio, where the monthly-averaged SST perturbations tend, on average, to be smaller in magnitude than in the other three regions. The geographical differences in α_v between the four regions are likely due to geographic differences in the vertical structure of the boundary layer and large-scale forcing. Seasonality of α_v is investigated from 5+ years of satellite data over these four regions (and the eastern tropical Pacific) in OCE.

Finally, we note that for SST perturbations warmer than about 1.5°, there is a subtle flattening of the bin-averaged V' relative to the linear fit, particularly over the South Atlantic and Agulhas Return Current regions. Interestingly, this flattening does not occur over cool SST perturbations. This difference between the bin-averaged V' and the linear fit is less than about 0.25 m s^{-1}, and there are very few data points in these outer bins, as shown by the histograms in Fig. 3. Because this flattening

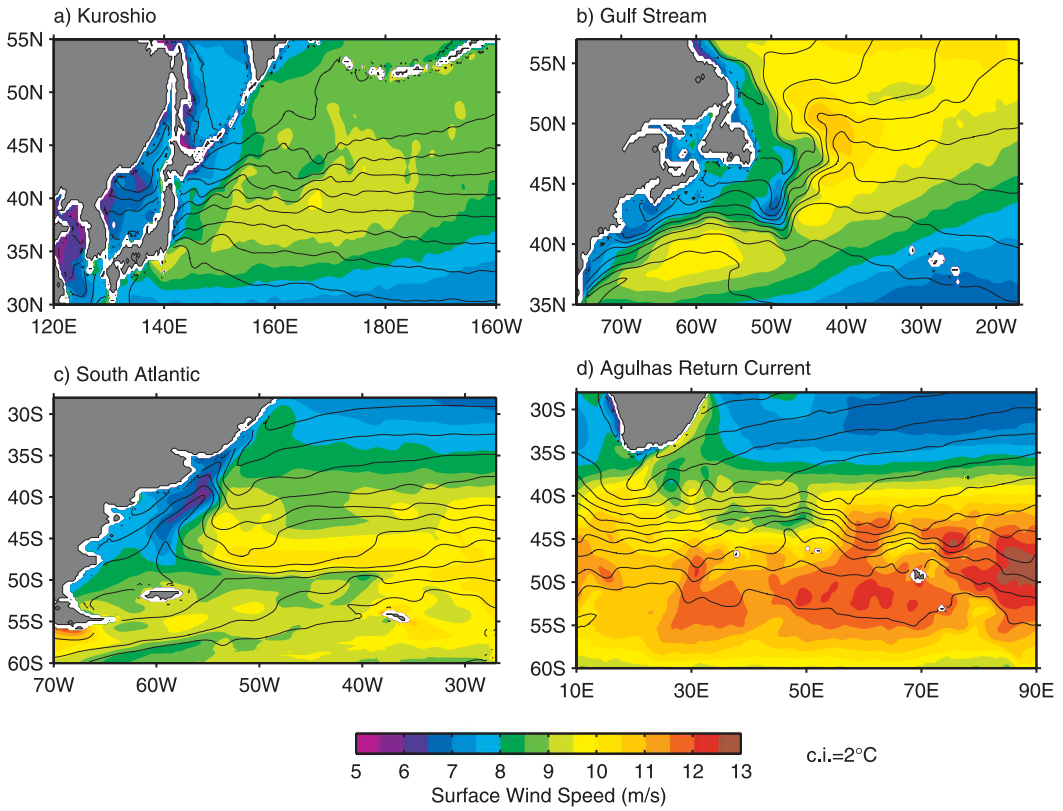

FIG. 2. Maps of the unfiltered QuikSCAT wind speed (colors) and AMSR-E SST (contours) scalar-averaged over the period June 2002–August 2008. The SST contour interval is 2°C.

of V' is relatively small and affects only a very small percentage of the observations, it does not significantly affect the analysis presented here. This observation is currently the subject of ongoing analysis.

b. *Wind direction response to SST*

The wind direction over these four regions is shown in Fig. 4 by the streamlines of the vector-averaged surface wind from QuikSCAT for the 75-month period considered here. The surface flow in all four regions has a strong westerly component, characteristic of typical midlatitude surface flow. The flow immediately downstream of the Asian and North American continents has a significant northerly component before gradually turning northward far offshore. Over the Southern Hemisphere regions, the flow is westerly poleward of the large-scale subtropical anticyclones located near 30°–35°S.

For quantitative purposes, it is desirable here to consider wind direction perturbations analogous to the spatially high-pass filtered wind speed perturbations investigated in section 4a. However, scalar wind direction cannot be spatially high-pass filtered in the same manner as wind speed in regions straddling absolute jumps in wind direction exceeding 360° and where the wind speed approaches zero, in which case the wind direction becomes undefined. Both cases occur intermittently in each of the four regions under consideration. To avoid these difficulties, mesoscale wind direction perturbations are defined here as the counterclockwise angle between the unfiltered $\mathbf{u}$ and the spatially low-pass filtered $\tilde{\mathbf{u}}$, where the tilde represents spatial low-pass filtering. These wind direction perturbations were computed from vector-averaged wind components at monthly intervals only at points where the magnitude of the monthly vector-averaged wind speed exceeded 1 m s^{-1}.

Spatial maps of the so-defined mesoscale wind direction perturbations scalar-averaged over the 75-month analysis period are shown in Fig. 5 along with contours of the

TABLE 2. The (left) coupling coefficient α_v and (right) spatial correlation coefficient computed from the monthly-averaged perturbation QuikSCAT wind speed and AMSR-E SST fields.

	α_v [m s^{-1} (°C)$^{-1}$]	Correlation coefficient
Kuroshio	0.30	0.70
Gulf Stream	0.27	0.79
South Atlantic	0.43	0.87
Agulhas	0.49	0.83

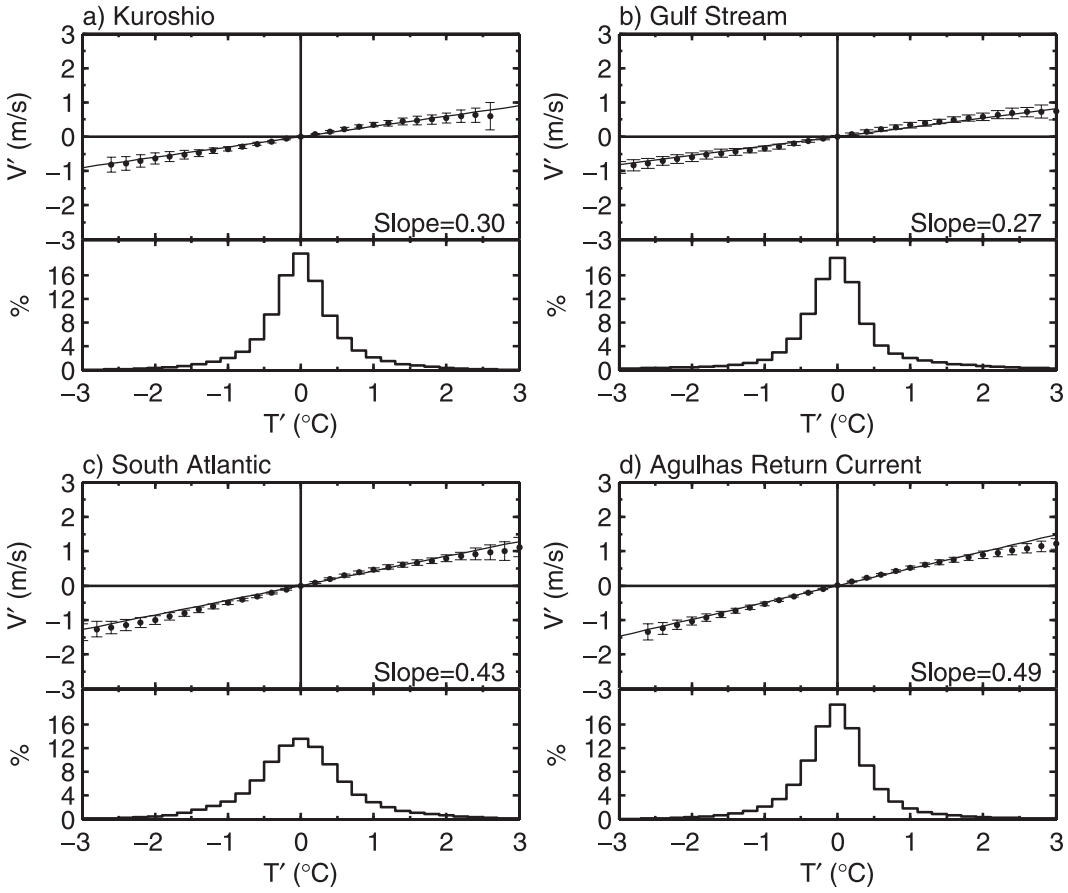

FIG. 3. Binned scatterplots of the spatially high-pass filtered QuikSCAT wind speed (V') as a function of the spatially high-pass filtered AMSR-E SST (T'). The bin averages were computed from monthly-averaged QuikSCAT wind and AMSR-E SST fields over the 75-month analysis period using all available data points in the regions enclosed in Figs. 1 and 2. The points and error bars represent the means and standard deviations within each bin, respectively, and the dashed lines are linear least squares fits to the means within each bin. Below each scatterplot, a histogram of the spatially high-pass filtered AMSR-E SST is included for reference.

AMSR-E perturbation SST. Perhaps the most striking feature of these wind direction perturbations is the pronounced meridional displacement of the wind direction perturbations relative to those of SST. In the Northern Hemisphere, negative wind direction perturbations are shifted north of warm SST perturbations and positive wind direction perturbations are shifted north of cool SST perturbations. Conversely, in the Southern Hemisphere, positive wind direction perturbations are shifted south of warm SST perturbations and negative wind direction perturbations are shifted south of cool SST perturbations.

Meridional displacements of the wind direction perturbations relative to those of SST that are qualitatively evident in Fig. 5 preclude the use of simple binned averages to statistically quantify the relationship between wind direction and SST such as was performed with the wind speed perturbations in section 4a (Fig. 3). Statistical relationships between the wind direction and SST perturbations can nonetheless be obtained here through cross-spectral analysis of the wind direction and SST perturbations in the meridional wavenumber domain. Estimates of cross-spectral statistics (squared coherence, transfer function, and phase spectra as functions of meridional wavenumber) were computed at monthly intervals along continuous meridional segments within each of the four regions and then ensemble averaged over all 75 months and segments (Fig. 6).

The squared coherence is largest over the South Atlantic and Agulhas Return Current, where perturbation SST variability accounts for 10%–15% of the meridional variance in the perturbation wind direction. Over the Gulf Stream and Kuroshio, the squared coherence is below 0.05. Wind direction perturbations are therefore less well correlated with SST compared with wind speed. The transfer function represents an estimate of the coupling coefficient between the perturbation wind direction

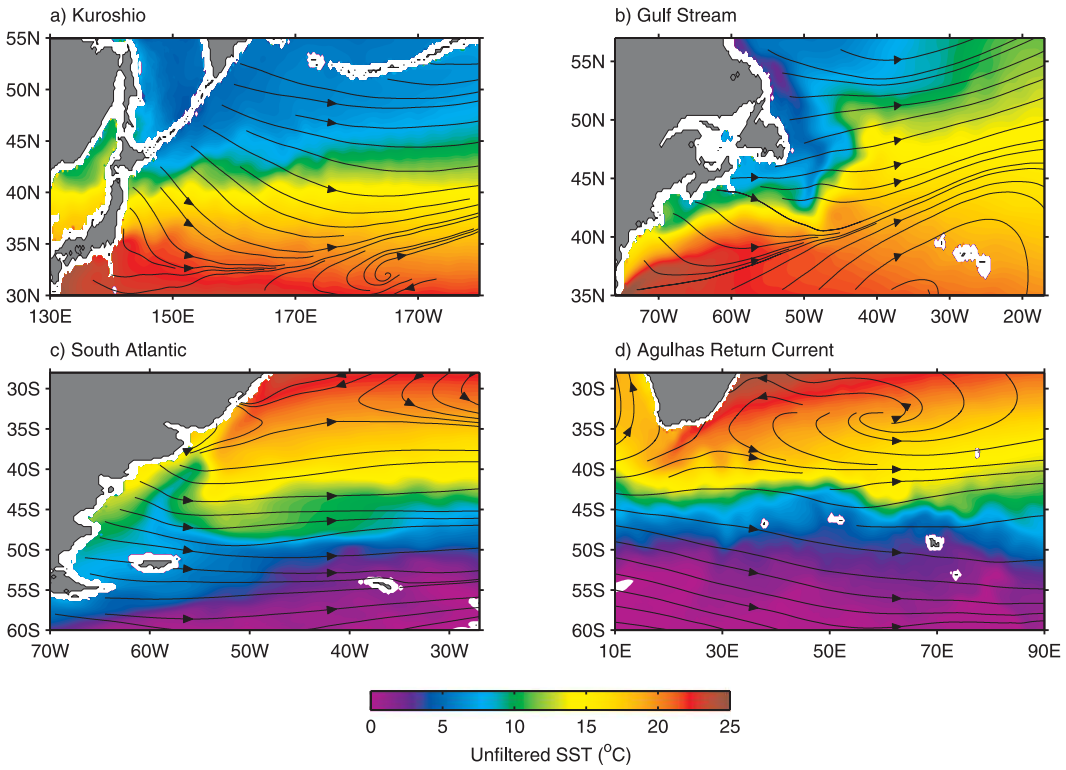

FIG. 4. Maps of the unfiltered AMSR-E SST (colors) scalar-averaged over the period June 2002–August 2008 for the four regions considered in this study. Overlaid are select streamlines of the surface flow computed from the 75-month vector-averaged QuikSCAT winds, where the arrows indicate flow direction.

and SST as a function of meridional wavenumber. From the transfer function in Fig. 6, the linear responses of the wind direction perturbations are roughly 2° per degree Celsius change in perturbation SST over all four regions and vary little with meridional wavenumber. SST-induced wind direction perturbations are thus about 4°–8° for a 2°–4°C change in perturbation SST, which is consistent with the magnitude of the wind direction perturbations evident in Fig. 5. The meridional phase spectrum is a measure of the meridional phase difference as a function of meridional wavenumber. Over all four regions, the phase spectra vary approximately linearly with wavenumber, indicative of a constant meridional displacement between the wind direction and SST perturbations. The meridional displacement L_0 of the wind direction perturbations relative to the SST perturbations estimated from the slope of the phase spectra in Fig. 6 is poleward about 1° latitude over all four regions, consistent with the spatial lags evident visually in Fig. 5.

The influence of SST on wind direction has been shown qualitatively from previous case studies over the Gulf Stream using mesoscale atmospheric models (Song et al. 2006; Spall 2007b) and scatterometer observations of Gulf Stream rings (Park et al. 2006) and over the Southern Ocean from model simulations (Thum 2006; O'Neill et al. 2010) and aircraft observations (e.g., Jury 1994). The results in these studies are consistent with the results shown here based on 75 months of QuikSCAT wind and AMSR-E SST observations.

These observations of the SST-induced wind direction perturbations show that 1) wind direction perturbations are shifted poleward by about 1° latitude relative to the SST perturbations and 2) in the Northern (Southern) Hemisphere, warm SST perturbations induce negative (positive) wind direction perturbations and cool SST perturbations induce positive (negative) wind direction perturbations; the magnitude of these wind direction perturbations is about 2° per degree Celsius change in perturbation SST over all four regions.

The wind vector responses to meanders in SST fronts are summarized schematically in Fig. 7 for each hemisphere. For illustrative purposes, the meridional displacement of the wind direction perturbations relative to the SST front are not shown here because they are small relative to the overall meridional extent of the SST perturbations, which is typically 3°–5° latitude. Note that for surface flow from cool to warm SST, the surface winds turn anticyclonically, whereas for surface flow

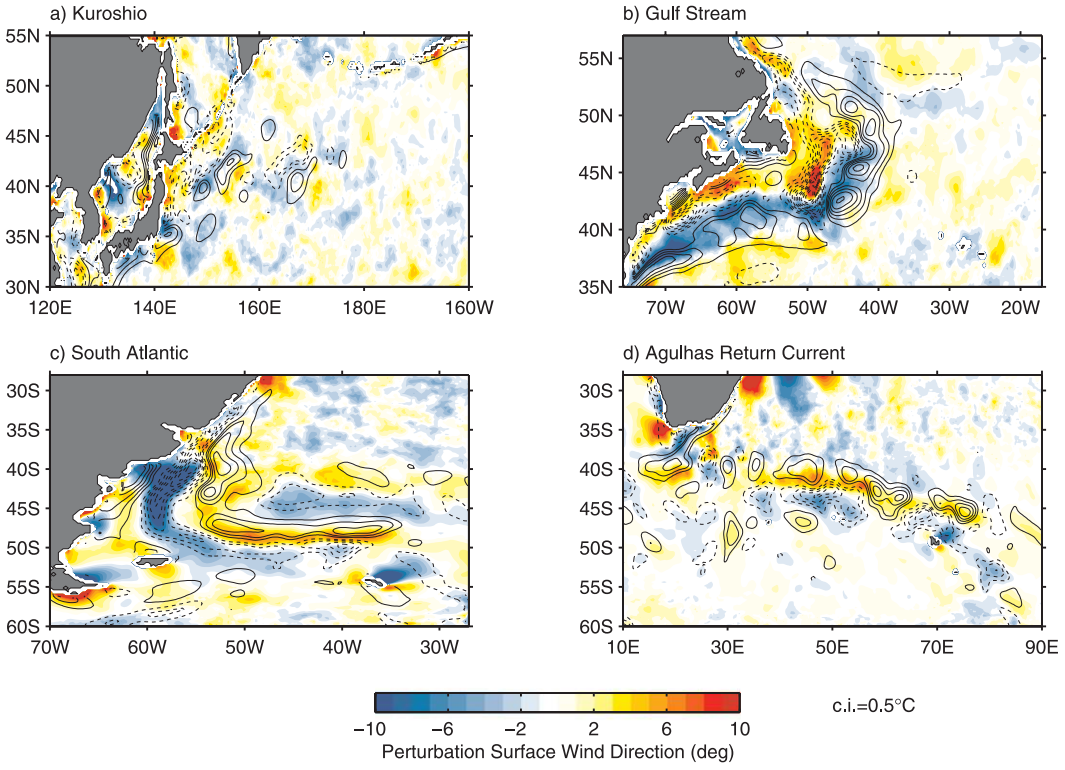

FIG. 5. As in Fig. 1, but for the QuikSCAT perturbation wind direction scalar averaged over the period June 2002–August 2008. As discussed in the text, wind direction perturbations are defined here as the counterclockwise angle between the unfiltered and spatially low-pass filtered surface wind vectors.

from warm to cool SST, the surface winds turn cyclonically.[2] Although the coupling between wind direction and SST is weaker than the coupling between wind speed and SST, it nonetheless has important consequences for the surface vorticity and divergence fields, as will be discussed below. Small changes in wind direction over short distances produce relatively large vorticity and divergence perturbations, as demonstrated below.

5. SST-induced variability in the surface vorticity and divergence fields

The separate effects of spatial gradients in wind speed and direction on the vorticity and divergence fields are ascertained by expressing the vorticity and divergence in curvilinear natural coordinates (e.g., Haltiner and Martin 1957):

$$\nabla \times \mathbf{u}' = -\left(\frac{\partial V}{\partial n}\right)' + \left(V\frac{\partial \psi}{\partial s}\right)', \tag{3}$$

$$\nabla \cdot \mathbf{u}' = \left(\frac{\partial V}{\partial s}\right)' + \left(V\frac{\partial \psi}{\partial n}\right)', \tag{4}$$

where (s, n) are the local downwind and crosswind coordinates, respectively. Equation (3) partitions the perturbation vorticity field[3] into the difference between the local crosswind speed gradient and a term related to the local downwind gradient in flow direction. Likewise, Eq. (4) partitions the perturbation divergence field into the sum of the downwind speed gradient and a term related to the crosswind gradient in flow direction. The direction gradient term in the vorticity is related to the radius of curvature of surface streamlines, whereas the direction gradient term in the divergence is related to spreading or contracting of streamlines in the crosswind direction, which is often referred to as the diffluent tendency (Haltiner and Martin 1957). Decomposing the vorticity and divergence in this manner allows investigation of the separate effects of lateral shear and downwind

[2] Anticyclonic rotation is clockwise in the Northern Hemisphere and counterclockwise in the Southern Hemisphere. Cyclonic rotation is the opposite of this.

[3] The horizontal vorticity should be expressed formally as $(\nabla \times \mathbf{u}) \cdot \hat{k}$. The expression $\nabla \times \mathbf{u}$ is used as shorthand for this to simplify the mathematical notation throughout the rest of this analysis.

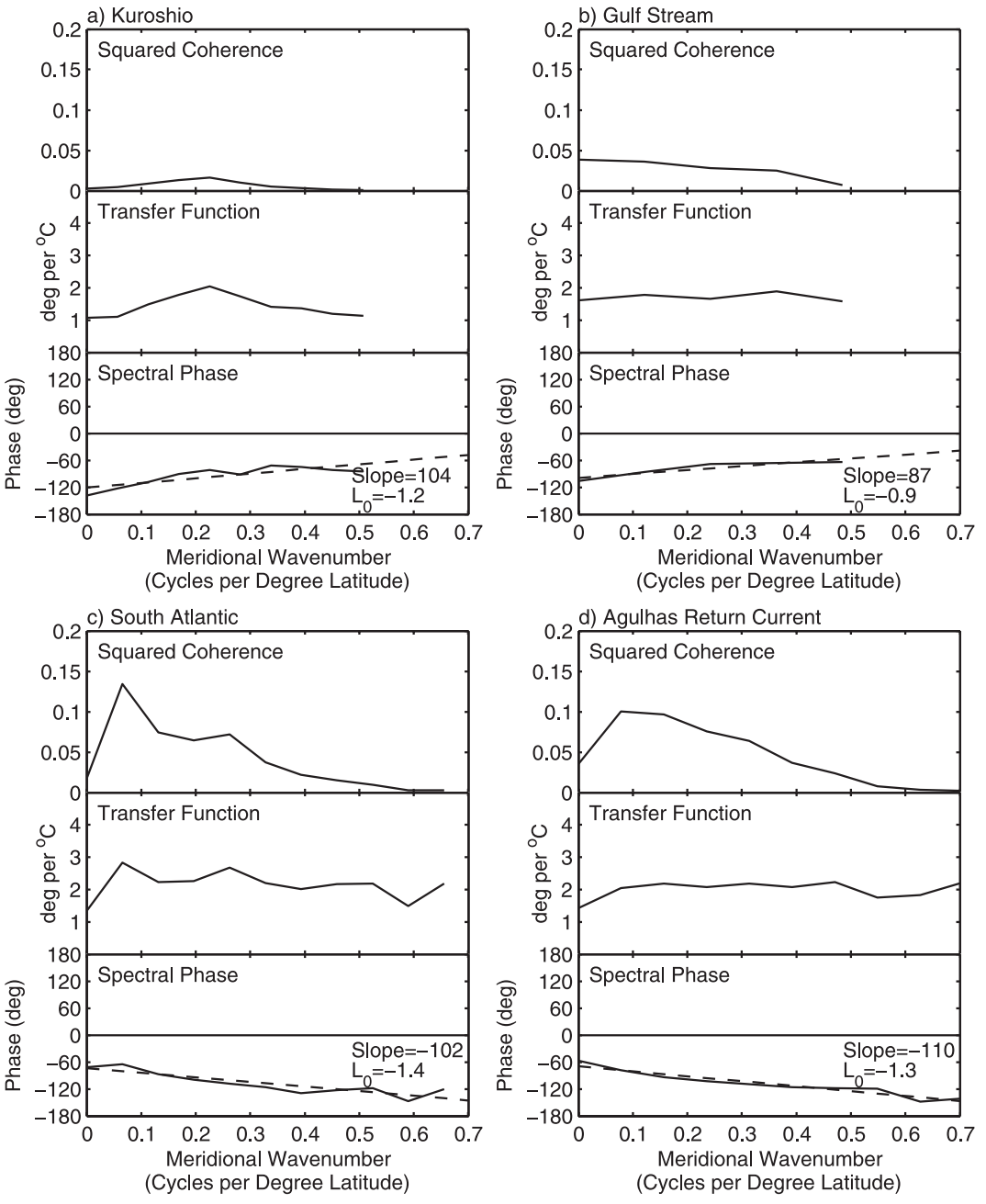

FIG. 6. Cross-spectral statistics of the perturbation wind direction dependence on the perturbation SST as a function of meridional wavenumber: (top) squared coherence, (middle) transfer function, and (bottom) phase spectra. Only cross-spectral estimates at wavenumbers with squared coherences above the 95% confidence level are shown. The dashed lines in the phase spectra plots are linear least squares fits of the phase estimates with slopes as indicated. These are used to compute estimates of the meridional displacement L_0 between wind direction and SST perturbations, which are indicated in each panel; the units of L_0 shown are in degrees latitude.

rotation on the vorticity and the separate effects of downwind acceleration and crosswind rotation on the divergence.

Crosswind and downwind wind speed gradients were computed in-swath using

$$\left(\frac{\partial V}{\partial n}\right)' = \left(-\sin\psi\frac{\partial V}{\partial x} + \cos\psi\frac{\partial V}{\partial y}\right)' \quad \text{and}$$

$$\left(\frac{\partial V}{\partial s}\right)' = \left(\cos\psi\frac{\partial V}{\partial x} + \sin\psi\frac{\partial V}{\partial y}\right)'.$$

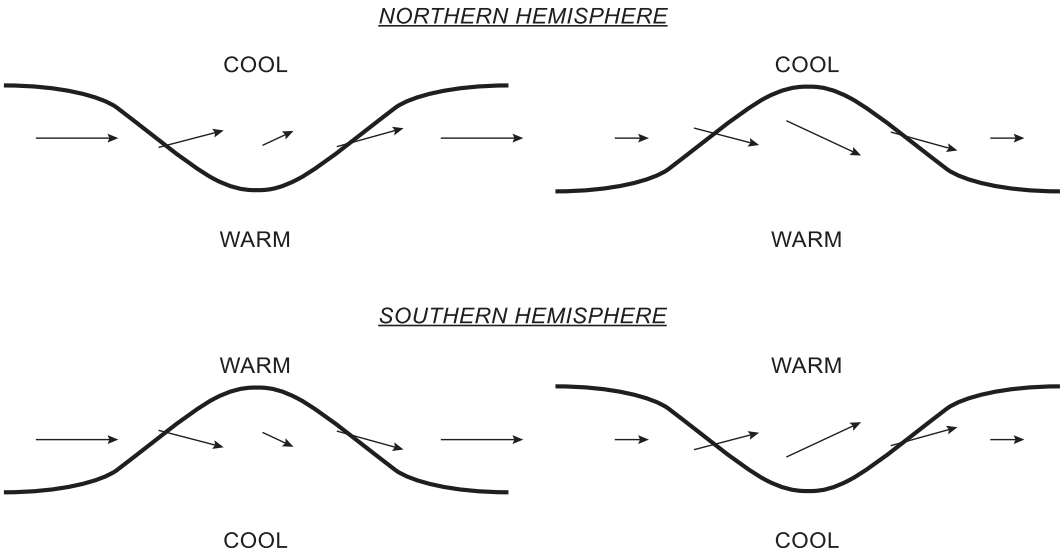

FIG. 7. Summary schematic of the vector wind response to meanders along an extratropical SST front, represented here by the solid curves, as deduced from the wind speed and direction dependencies on SST. Whereas the wind speed response to SST (as represented by the relative length of the vectors) is the same for both hemispheres, the wind direction response to SST (as represented by the relative turning of the vectors) differs in sign between the Northern and Southern Hemispheres.

The crosswind and downwind direction gradients were computed from the gridded vorticity, divergence, and speed gradient fields using

$$\left(V\frac{\partial\psi}{\partial n}\right)' = \left(\nabla\cdot\mathbf{u} - \frac{\partial V}{\partial s}\right)' \quad \text{and}$$

$$\left(V\frac{\partial\psi}{\partial s}\right)' = \left(\nabla\times\mathbf{u} + \frac{\partial V}{\partial n}\right)'.$$

a. *Spatial gradients of perturbation wind speed and SST*

From the linear statistical relationship between V' and T' expressed by Eq. (2), it follows that crosswind and downwind gradients of wind speed should depend, respectively, on the crosswind and downwind components of the SST gradient field such that

$$\left(\frac{\partial V}{\partial n}\right)' = \alpha_c^{\mathrm{spd}}\left(\frac{\partial T}{\partial n}\right)' \quad \text{and} \tag{5}$$

$$\left(\frac{\partial V}{\partial s}\right)' = \alpha_d^{\mathrm{spd}}\left(\frac{\partial T}{\partial s}\right)', \tag{6}$$

where α_c^{spd} and α_d^{spd} are the coupling coefficients for the speed gradient responses to the SST gradients. The QuikSCAT crosswind and downwind speed gradient components are indeed related linearly to the crosswind and downwind SST gradient components, respectively, for the 75-month period of interest here (Fig. 8). Moreover, within each region α_c^{spd} and α_d^{spd} are nearly equal to α_v from Fig. 3. The scalar wind speed and speed gradient responses to mesoscale SST perturbations therefore appear to be manifestations of the same physical mechanisms. This strong coupling between the crosswind and downwind speed and SST gradients is further illustrated in the maps of the perturbation crosswind and downwind speed and SST gradients averaged over the 75-month period (Fig. 9). The corresponding cross-correlation coefficients between these time-averaged fields are shown in Table 3; they are comparable to those of the wind speed and SST perturbations presented in Table 2 for the Southern Hemisphere, while being somewhat weaker in the Northern Hemisphere. Note that in the core of the Gulf Stream region near 37°N, 70°W, there is little signal in the downwind speed gradients even though the downwind SST gradients are strong. This may be due to the effects of the strong Gulf Stream ocean surface currents on the scatterometer winds, as argued in Fig. 5 of Chelton et al. (2004).

The linear relationships between the perturbation wind speed and SST fields can be investigated further by expressing the perturbation crosswind and downwind components of the SST gradient as

$$\left(\frac{\partial T}{\partial n}\right)' = M_T\sin\theta' \quad \text{and}$$

$$\left(\frac{\partial T}{\partial s}\right)' = M_T\cos\theta', \tag{7}$$

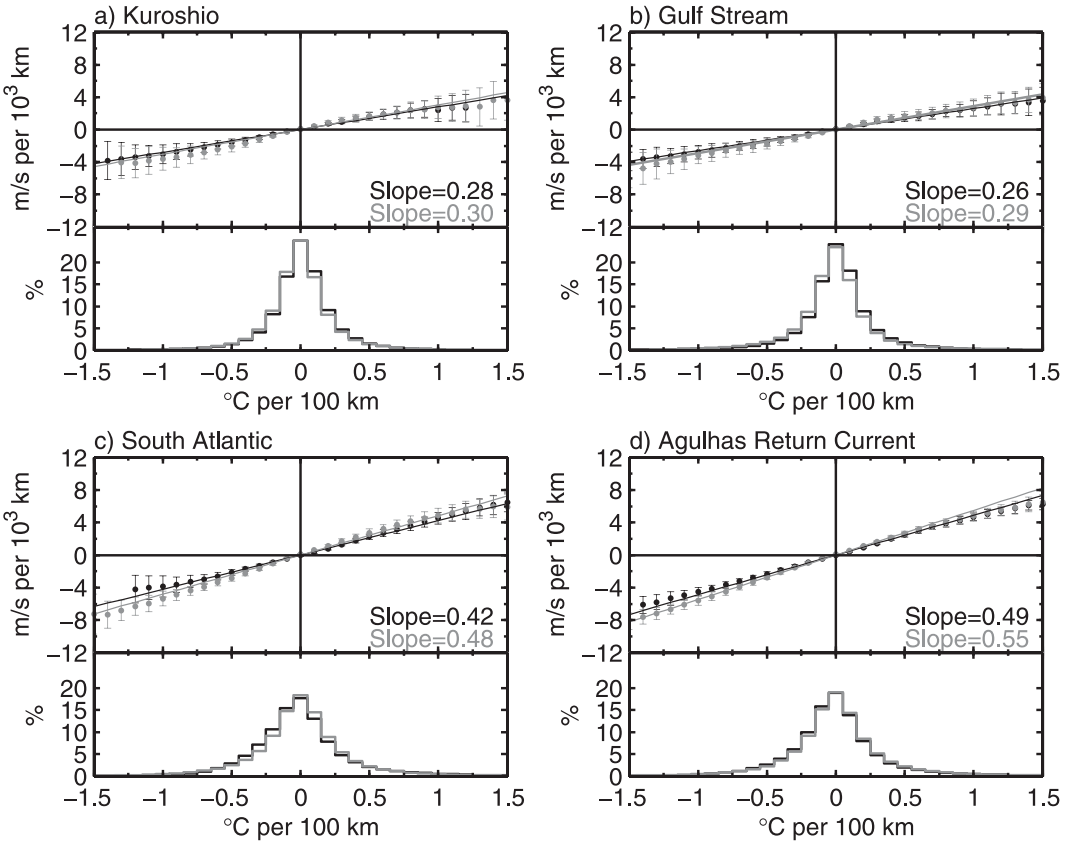

FIG. 8. As in Fig. 3, but for the QuikSCAT perturbation crosswind speed gradient $(\partial V/\partial n)'$ binned as a function of the crosswind SST gradient $(\partial T/\partial n)'$ (black) and the QuikSCAT perturbation downwind speed gradient $(\partial V/\partial s)'$ binned as a function of the downwind SST gradient $(\partial T/\partial s)'$ (gray).

where the perturbation SST gradient magnitude M_T and the angle θ' are defined such that

$$M_T = \sqrt{\left(\frac{\partial T}{\partial s}\right)'^2 + \left(\frac{\partial T}{\partial n}\right)'^2} \quad \text{and}$$

$$\theta' = \tan^{-1}\frac{(\partial T/\partial n)'}{(\partial T/\partial s)'}. \tag{8}$$

Geometrically, θ' closely approximates the angle between the surface streamlines of the unfiltered surface winds and the perturbation SST gradient vector $\nabla T'$ (justification of this physical interpretation of θ' is given in the appendix). From consideration of the simple linear relationship between the perturbation wind speed and SST in Eq. (2), the largest downwind speed gradients should occur as surface winds blow across perturbation SST isotherms such that the wind speed increases as winds blow from cool to warm water when $\theta' = 0°$, resulting in $(\partial V/\partial s)' > 0$ in accord with Eq. (6), and decreases as winds blow from warm to cool water when $\theta' = \pm 180°$, resulting in $(\partial V/\partial s)' < 0$. Likewise, the largest crosswind speed gradients should occur as the surface winds blow along perturbation SST isotherms (when $\theta' = \pm 90°$).

The angular dependencies of the perturbation crosswind and downwind speed gradients on θ' are shown in Fig. 10. The crosswind and downwind speed gradients closely follow sine and cosine functions, respectively, of the angle θ', in agreement with the hypothesized dependencies relating the wind speed gradients to the orientation of the surface streamlines relative to the perturbation SST isotherms. Close inspection of Fig. 10 reveals small but consistent phase shifts from the expected pure cosine curves. From these statistical results, we may thus express the crosswind and downwind speed gradients as

$$\left(\frac{\partial V}{\partial n}\right)' = \alpha_c^{\text{spd}} M_T \sin(\theta' + \phi_c^{\text{spd}}) \quad \text{and} \tag{9}$$

$$\left(\frac{\partial V}{\partial s}\right)' = \alpha_d^{\text{spd}} M_T \cos(\theta' + \phi_d^{\text{spd}}), \tag{10}$$

where α_c^{spd} and α_d^{spd} are the slopes of the speed gradient responses to the SST gradients shown in Fig. 8 and ϕ_c^{spd}

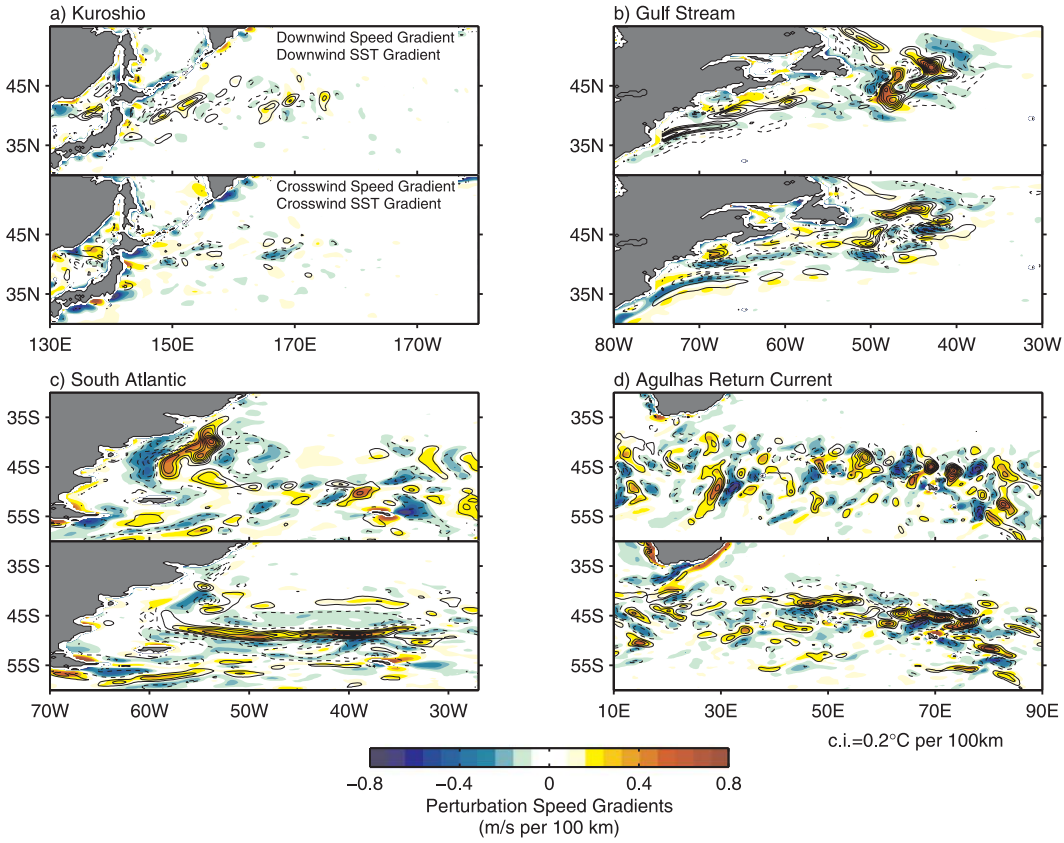

FIG. 9. (top maps in each panel) The perturbation crosswind speed gradient (colors) overlaid with contours of the crosswind SST gradient. (bottom maps in each panel) The perturbation downwind speed gradient (colors) overlaid with contours of the downwind SST gradient. The data in each map were averaged over the 75-month period June 2002–August 2008. The contour interval for the perturbation crosswind and downwind SST gradients is 0.2°C per 100 km, and the zero contour has been omitted for clarity. Solid and dashed contours correspond to positive and negative values of the SST gradient, respectively.

and ϕ_d^{spd} are the phase shifts of the sinusoidal responses of the speed gradients to θ' shown in Fig. 10 (positive for counterclockwise rotation). The values of the amplitudes and phase shifts are shown in Table 4. Within each region, α_c^{spd} and α_d^{spd} are nearly equal. Note that ϕ_c^{spd} is essentially 0° over all four regions whereas α_d^{spd} is 8°–17° with opposing signs between hemispheres.

b. *SST-induced speed and direction gradient effects on vorticity and divergence*

The perturbation vorticity and divergence fields binned as functions of the perturbation crosswind and downwind SST gradients, respectively, are shown in Fig. 11. The perturbation vorticity and divergence fields are highly correlated with small-scale perturbations in the SST gradient field, as demonstrated in our previous studies using the wind stress curl and divergence fields (Chelton et al. 2001, 2004, 2007; O'Neill et al. 2003, 2005). To emphasize the difference between the vorticity and divergence responses, and for consistency with our previous studies, the vorticity is binned as a function of the negative crosswind SST gradient $-(\partial T/\partial n)'$ in Fig. 11. In agreement with these previous studies shown in Table 1, the magnitude of the slope of the divergence response to downwind SST gradients is significantly larger than that of the vorticity response to crosswind SST gradients. Additionally, the variability within each bin, as represented by the standard deviation within each bin, is much smaller for the speed gradient components in Fig. 8 than for the vorticity and divergence in Fig. 11. This is evidently because contributions of the SST-induced wind direction responses to the vorticity and divergence are noisier than the wind speed responses.

Given the results of section 3a and Eqs. (3) and (4), if the surface vorticity and divergence were dependent only on the crosswind and downwind speed gradients, respectively, then the slopes of the straight line fits in Fig. 11 should be equal in magnitude but opposite in sign. Evidently, the direction gradient terms in Eqs. (3) and (4) reduce the overall vorticity responses to crosswind

TABLE 3. Cross-correlation coefficients between the various perturbation derivative wind fields and the perturbation crosswind and downwind SST gradient components as indicated. These correlation coefficients were computed from the derivative wind and SST fields averaged over the 75-month analysis period at monthly intervals.

	Kuroshio	Gulf Stream	South Atlantic	Agulhas
$\nabla \times \mathbf{u}'$ and $\left(\frac{\partial T}{\partial n}\right)'$	−0.16	−0.25	−0.46	−0.57
$\nabla \cdot \mathbf{u}'$ and $\left(\frac{\partial T}{\partial s}\right)'$	0.49	0.62	0.72	0.82
$\left(\frac{\partial V}{\partial n}\right)'$ and $\left(\frac{\partial T}{\partial n}\right)'$	0.33	0.52	0.72	0.79
$\left(\frac{\partial V}{\partial s}\right)'$ and $\left(\frac{\partial T}{\partial s}\right)'$	0.50	0.56	0.79	0.86
$\left(V\frac{\partial \psi}{\partial s}\right)'$ and $\left(\frac{\partial T}{\partial s}\right)'$	−0.18	−0.31	0.61	0.60
$\left(V\frac{\partial \psi}{\partial n}\right)'$ and $\left(\frac{\partial T}{\partial n}\right)'$	−0.27	−0.37	0.68	0.69

SST gradients and enhance the divergence responses to downwind SST gradients. This point is addressed in detail in section 4c.

Besides these differences, there are significant differences in the vorticity and divergence dependencies on θ' (Fig. 12) from that expected solely from consideration of SST-induced wind speed perturbations. In our previous work, we hypothesized that the surface curl should depend on the sine of θ' whereas the divergence should depend on the cosine of θ'. Inspection of the vorticity and divergence dependencies on θ' in Fig. 12, however, reveals that the vorticity and divergence do not depend exactly on the sine and cosine, respectively, of θ' but rather are phase shifted (Fig. 12). The values of the phase shifts are labeled on Fig. 12. These phase shifts have absolute magnitudes of approximately 25° for the vorticity and 10° for the divergence in all four regions but with opposite signs in each hemisphere. As addressed below, these phase shifts and the amplitude differences in Fig. 11 (also evident from the amplitudes of the sinusoids in Fig. 12) can be related directly to the influence of SST on the direction gradient terms in Eqs. (3) and (4).

The dependence of the direction gradient terms on SST can be ascertained conceptually from the schematic in Fig. 7. When the surface flow is from cool to warm SST, the surface winds turn anticyclonically, whereas for surface flow from warm to cool SST the surface winds turn cyclonically. This observation suggests that the downwind gradient in wind direction $V(\partial\psi/\partial s)$ should depend on the downwind SST gradient and hence on the cosine of θ'. Additionally, crosswind direction gradients $V(\partial\psi/\partial n)$ should form as the wind blows along perturbation SST isotherms in association with the crosswind SST gradient and will thus depend on the sine of θ'.

The time-averaged maps of the perturbation downwind direction and SST gradients and the perturbation crosswind direction and SST gradients in Fig. 13 indeed show a correlation between the direction gradient and SST gradients consistent with these hypothesized dependencies. The poleward displacement of the wind direction perturbations relative to those of SST discussed in section 4b is also evident in these maps. The correlations are weakest over the Kuroshio and strongest in the Southern Hemisphere regions, as quantified by the cross-correlation coefficients between the crosswind and downwind direction gradients and the crosswind and downwind SST gradients, respectively, in Table 3. Additionally, the magnitudes of the correlation coefficients between the downwind direction gradients and the downwind SST gradients are consistently smaller than those between the crosswind direction gradients and the crosswind SST gradients. However, both are much smaller than the correlations between the crosswind and downwind gradients of wind speed and SST, thus explaining the higher variability of the vorticity and divergence binned averages in Fig. 11 compared with the speed-only contributions to the vorticity and divergence in Fig. 8.

The dependencies of the direction gradient terms on θ' quantified statistically in Fig. 14 confirm that the crosswind and downwind direction gradients vary as the sine and cosine of θ', respectively. As expected in all four regions, the downwind direction gradient response to θ' (gray curve in Fig. 14) shows that the surface wind tends to rotate anticyclonically when the large-scale flow is from cool to warm water (i.e., when $\theta' = 0°$) and cyclonically when the large-scale flow is from warm to cool water (i.e., when $\theta' = \pm 180°$). The crosswind direction gradient response to θ' indicates a maximum surface diffluent tendency as winds blow approximately along perturbation SST isotherms (i.e., when $\theta' = \pm 90°$).

Statistically, the direction gradient terms can thus be represented by

$$\left(V\frac{\partial \psi}{\partial s}\right)' = \alpha_d^{\mathrm{dir}} M_T \cos(\theta' - \phi_d^{\mathrm{dir}}) \quad \text{and} \tag{11}$$

$$\left(V\frac{\partial \psi}{\partial n}\right)' = \alpha_c^{\mathrm{dir}} M_T \sin(\theta' + \phi_c^{\mathrm{dir}}), \tag{12}$$

where α_d^{dir} and α_c^{dir} are coupling coefficients for the downwind and crosswind direction gradients, respectively, and ϕ_d^{dir} and ϕ_c^{dir} are phase shifts (see Table 4). These statistical relations, along with the statistical relations for the speed gradients in Eqs. (9) and (10), are used in section 4c to aid in understanding the differences between

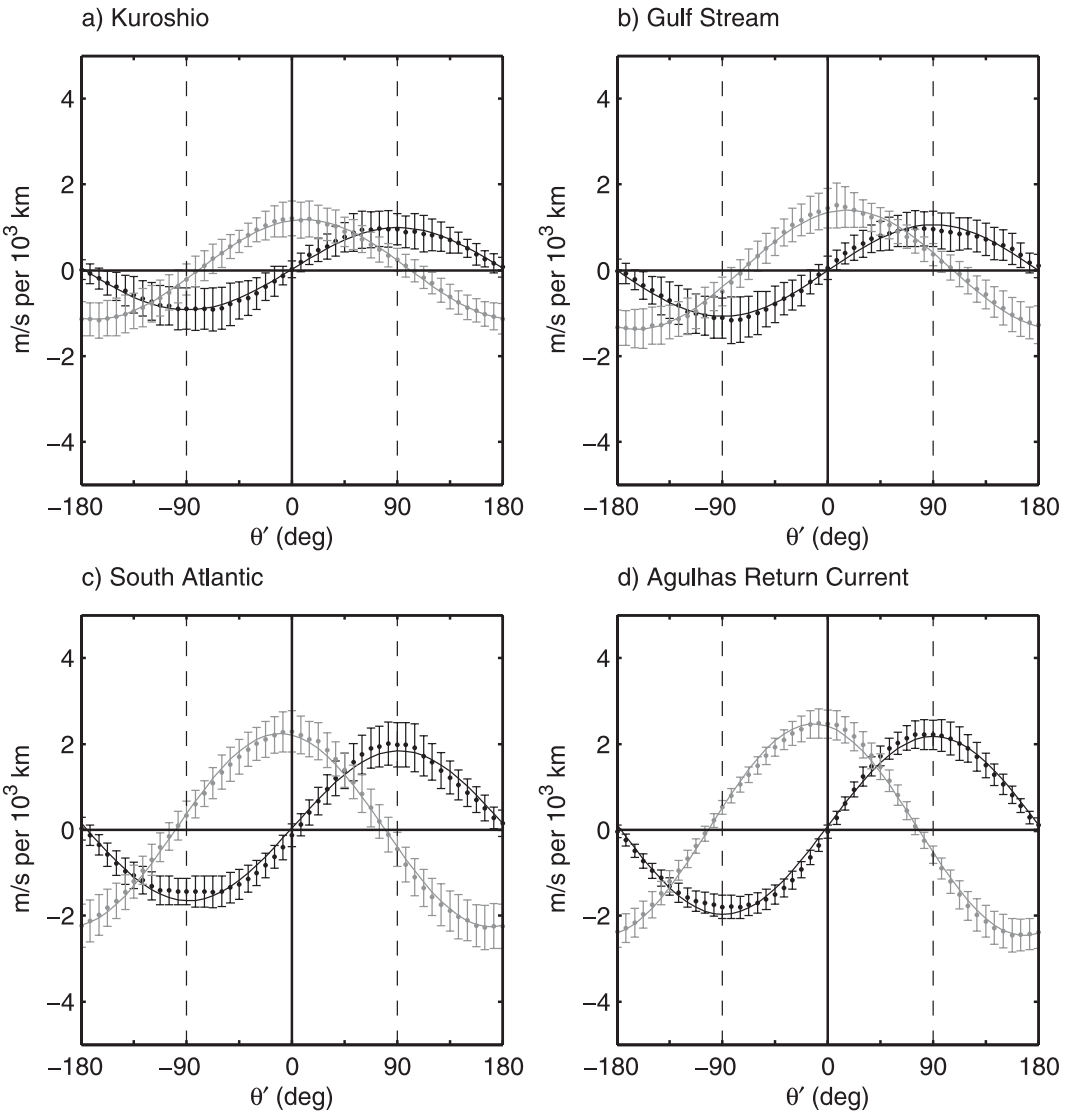

FIG. 10. Binned scatterplots of the perturbation crosswind (black) and downwind (gray) speed gradients as functions of θ'. The bin averages were computed from monthly-averaged QuikSCAT wind and AMSR-E SST fields over the 75-month period considered here using all available data points in the regions enclosed in Figs. 1 and 2. The points and error bars represent the means and standard deviations within each bin, respectively. The solid curves are least squares fits of the points to phase-shifted sinusoids.

the vorticity and divergence responses to the crosswind and downwind SST gradients.

c. *Why is the vorticity response to crosswind SST gradients weaker than the divergence response to downwind SST gradients?*

The statistical relations developed above provide an explanation of why the vorticity response to crosswind SST gradients is weaker than the divergence response to downwind SST gradients. Recall that the vorticity and divergence dependencies on the crosswind and downwind SST gradients were interpreted conceptually from consideration of the effects of SST on wind speed only (Chelton et al. 2001, and our subsequent studies). From a qualitative perspective, the crosswind direction and downwind speed gradient responses to θ' (the black and gray curves in Figs. 14 and 10, respectively) are nearly in phase, yielding a larger amplitude divergence response to θ' than that of the downwind speed gradient alone; in contrast, the downwind direction and negative crosswind speed gradient responses to θ' (the gray and black curves in Figs. 14 and 10, respectively) are nearly in antiphase, yielding a smaller-amplitude vorticity response to θ' than that of the crosswind speed gradient alone. The SST-induced direction

TABLE 4. Values of the coupling coefficients and phase angles appearing in Eqs. (13)–(18) computed from the QuikSCAT wind and AMSR-E SST fields. The units of the coupling coefficients are in m s^{-1} °C^{-1}.

	Kuroshio	Gulf Stream	South Atlantic	Agulhas
α_c^{spd}	0.28	0.26	0.42	0.49
α_d^{dir}	0.13	0.14	0.19	0.17
ϕ_c^{spd}	−3°	−5°	1°	2°
ϕ_d^{dir}	141°	146°	20°	23°
α_c^{vort}	−0.24	−0.22	−0.37	−0.45
α_d^{vort}	−0.089	−0.090	0.17	0.14
α_d^{spd}	0.30	0.29	0.48	0.55
α_c^{dir}	0.20	0.20	0.31	0.30
ϕ_d^{spd}	−11°	−17°	8°	12°
ϕ_c^{dir}	129°	138°	28°	28°
α_d^{div}	0.52	0.44	0.69	0.73
α_c^{div}	−0.057	−0.056	0.20	0.14

gradient perturbations thus enhance the divergence response to downwind SST gradients while simultaneously reducing the vorticity response to crosswind SST gradients.

This result can be shown more rigorously by noting that the crosswind and downwind speed gradient responses to θ' (Fig. 10) expressed in Eqs. (9) and (10) and the crosswind and downwind direction gradient responses to θ' (Fig. 14) expressed in Eqs. (11) and (12) can be combined to relate the vorticity and divergence fields to M_T and θ' as

$$\nabla \times \mathbf{u}' = \underbrace{-\alpha_c^{spd} M_T \sin(\theta' + \phi_c^{spd})}_{\text{Crosswind speed gradient}} + \underbrace{\alpha_d^{dir} M_T \cos(\theta' - \phi_d^{dir})}_{\text{Downwind direction gradient}}, \quad \text{and} \tag{13}$$

$$\nabla \cdot \mathbf{u}' = \underbrace{\alpha_d^{spd} M_T \cos(\theta' + \phi_d^{spd})}_{\text{Downwind speed gradient}} + \underbrace{\alpha_c^{dir} M_T \sin(\theta' + \phi_c^{dir})}_{\text{Crosswind direction gradient}}. \tag{14}$$

The components of the vorticity and divergence that each term represents empirically in these equations are indicated by the underbraces. Using trigonometric identities and rewriting these equations in terms of the crosswind and downwind SST gradients using Eq. (7) yields

$$\nabla \times \mathbf{u}' = \alpha_c^{vort}\left(\frac{\partial T}{\partial n}\right)' + \alpha_d^{vort}\left(\frac{\partial T}{\partial s}\right)' \quad \text{and}$$

$$\nabla \cdot \mathbf{u}' = \alpha_d^{div}\left(\frac{\partial T}{\partial s}\right)' + \alpha_c^{div}\left(\frac{\partial T}{\partial n}\right)',$$

where the set of coupling coefficients $(\alpha_c^{vort}, \alpha_d^{vort})$ and $(\alpha_d^{div}, \alpha_c^{div})$ are defined as

$$\alpha_c^{vort} = -\alpha_c^{spd}\cos\phi_c^{spd} + \alpha_d^{dir}\sin\phi_d^{dir}, \tag{15}$$

$$\alpha_d^{vort} = -\alpha_c^{spd}\sin\phi_c^{spd} + \alpha_d^{dir}\cos\phi_d^{dir}, \tag{16}$$

$$\alpha_d^{div} = \alpha_d^{spd}\cos\phi_d^{spd} + \alpha_c^{dir}\sin\phi_c^{dir}, \quad \text{and} \tag{17}$$

$$\alpha_c^{div} = -\alpha_d^{spd}\sin\phi_d^{spd} + \alpha_c^{dir}\cos\phi_c^{dir}. \tag{18}$$

Consider Eq. (15) for α_c^{vort}, which is the coupling coefficient for the vorticity response to the crosswind SST gradient. Both α_d^{dir} and $\sin\phi_d^{dir}$ are statistically found to be positive quantities (Table 4) over all four regions. Therefore, the downwind direction gradients reduce the vorticity response to crosswind SST gradients by a factor of $\alpha_d^{dir}\sin\phi_d^{dir}$. Likewise, from consideration of Eq. (17) for α_d^{div}, the crosswind direction gradients enhance the divergence response to downwind SST gradients by a factor of $\alpha_c^{dir}\sin\phi_c^{dir}$ since α_c^{dir} and $\sin\phi_c^{dir}$ are both found statistically to be positive quantities (Table 4) over all four regions. SST-induced wind direction gradients thus simultaneously reduce the vorticity response to crosswind SST gradients and enhance the divergence response to downwind SST gradients.

It is also noted that in coupled ocean–atmosphere simulations of tropical instability waves, Seo et al. (2007) and Small et al. (2009) have found that Ekman pumping anomalies associated with SST-induced wind stress curl perturbations tend to reduce the wind stress curl relative to the wind stress divergence perturbations. This apparently occurs because surface ocean currents tend to be quasi-nondivergent, thus affecting the wind stress curl more than the wind stress divergence. It is currently unknown whether similar ocean feedbacks act over midlatitudes to reduce the vorticity response to crosswind SST gradients in addition to the wind direction effects reported here.

6. Conclusions

Analysis of the differences between the surface vorticity and divergence responses to SST have revealed a significant response of the wind direction to mesoscale SST perturbations in addition to the well-known positive correlation and linear response of the surface wind speed to SST. Analysis of 75 months of QuikSCAT surface vector winds and AMSR-E SST observations showed that surface winds accelerate and turn anticyclonically when the surface flow is from cool to warm SST and decelerate and turn cyclonically when the surface flow is from warm to cool SST, with characteristic wind speed changes of 1–2 m s^{-1} and wind direction changes of 4°–8°. SST-induced wind direction perturbations are not collocated with SST perturbations, as is the case with the wind speed perturbations,

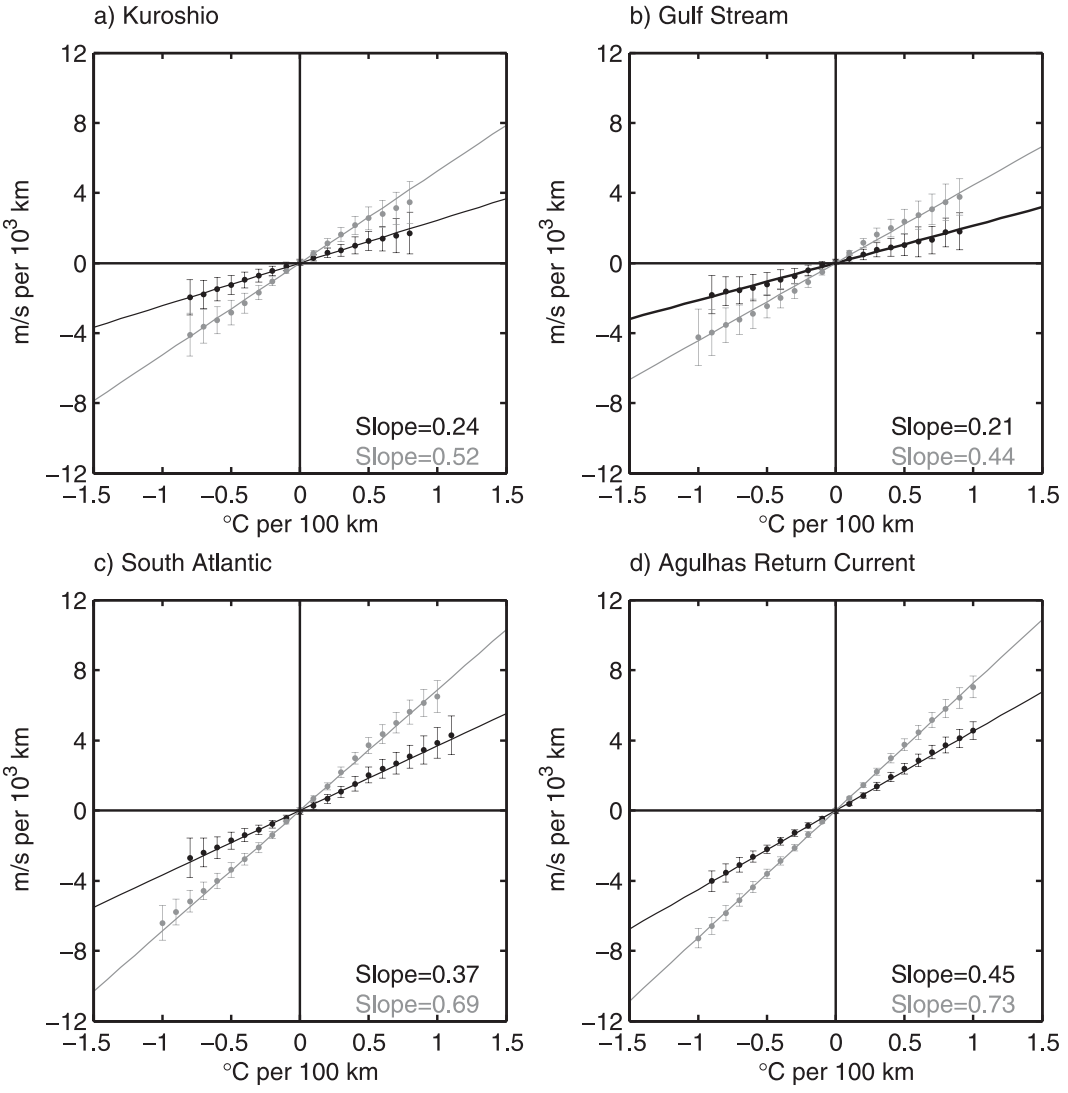

FIG. 11. As in Fig. 3, but for the QuikSCAT perturbation vorticity as a function of the negative perturbation crosswind SST gradient $-(\partial T/\partial n)'$ (black) and the QuikSCAT perturbation divergence as a function of the perturbation downwind SST gradient $(\partial T/\partial s)'$ (gray).

but are displaced poleward by about 1° latitude. The influence of mesoscale SST perturbations on surface wind direction has not been previously noted.

The vorticity and divergence perturbations are found to be related linearly to the crosswind and downwind components of the SST gradient, respectively, as in previous studies. The vorticity response to crosswind SST gradients is 30%–50% weaker than the divergence response to downwind SST gradients. Although this is the first study to consider the responses of the vorticity and divergence to SST, the results here are consistent with previous observational studies based on wind stress curl and divergence, as discussed in the introduction. By explicitly relating the vorticity and divergence to crosswind and downwind gradients of wind speed and direction using natural coordinates, we showed that although wind speed gradients contribute nearly equally to the vorticity and divergence responses to SST, the SST-induced wind direction contributions are diametrically opposed; SST-induced crosswind and downwind gradients in wind direction reduce the vorticity response to crosswind SST gradients while simultaneously enhancing the divergence response to downwind SST gradients.

The observational results shown here go a long way toward unifying the various statistical relationships observed among mesoscale perturbations of SST, wind speed, wind direction, vorticity, and divergence fields. At the heart of these interrelationships are the SST-induced

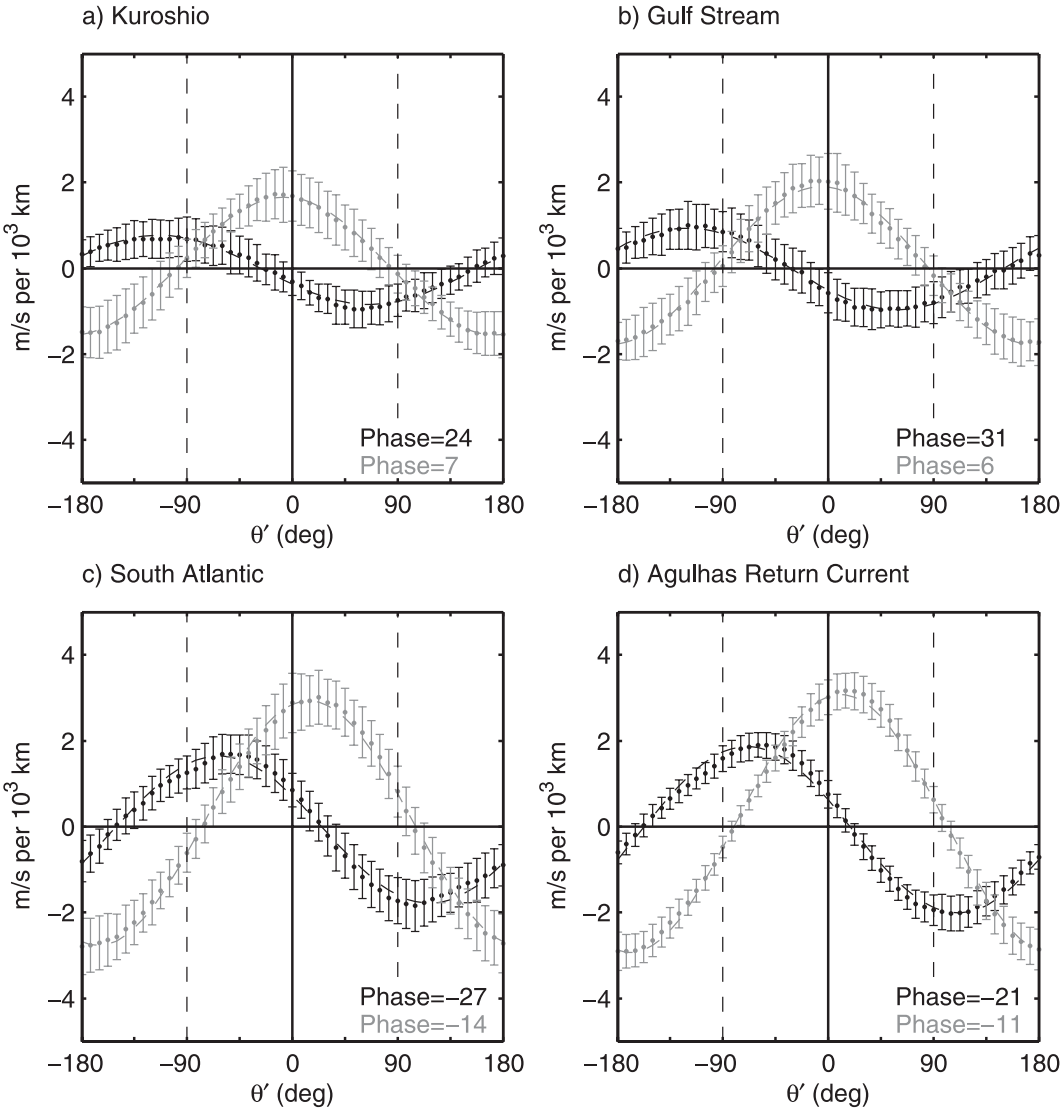

FIG. 12. As in Fig. 10, but for the QuikSCAT perturbation vorticity (black) and divergence (gray). The phase shifts relative to pure sine and cosine curves, respectively, are listed in the lower right of each panel, with units of degrees.

responses of the wind speed and direction to mesoscale SST perturbations. The relationships expressed here in terms of the surface wind speed and derivative wind fields have been extended to SST-induced perturbations of the corresponding wind stress fields (OCE). Because of the nonlinearity of the stress–wind relationship, spatially filtered perturbations of the wind stress curl, wind stress divergence, and wind stress magnitude are related to those of the vorticity, divergence, and wind speed, respectively, but are modulated by the strength of the ambient large-scale wind speed.

The feedback onto the ocean of the SST-induced wind stress curl and upper ocean mixing is the focus of ongoing research. It is becoming apparent that ocean circulation is significantly impacted by the presence of SST-induced mesoscale wind variability (e.g., Milliff et al. 1996; Seo et al. 2007; Spall 2007a; Jin et al. 2009; Hogg et al. 2009; Small et al. 2009). The statistical relations among vorticity, divergence, and SST developed here are being used to develop statistical parameterizations of the mesoscale surface wind stress response to temporally evolving SST fields in ocean models to simulate the effects of two-way coupling between the ocean and atmosphere. This method may be used to simulate mesoscale wind stress variability in long time series of surface wind stress analyses from numerical weather prediction models, which underestimate the SST influence on wind stress by about a factor of 2 (Maloney and Chelton 2006; Song et al. 2009).

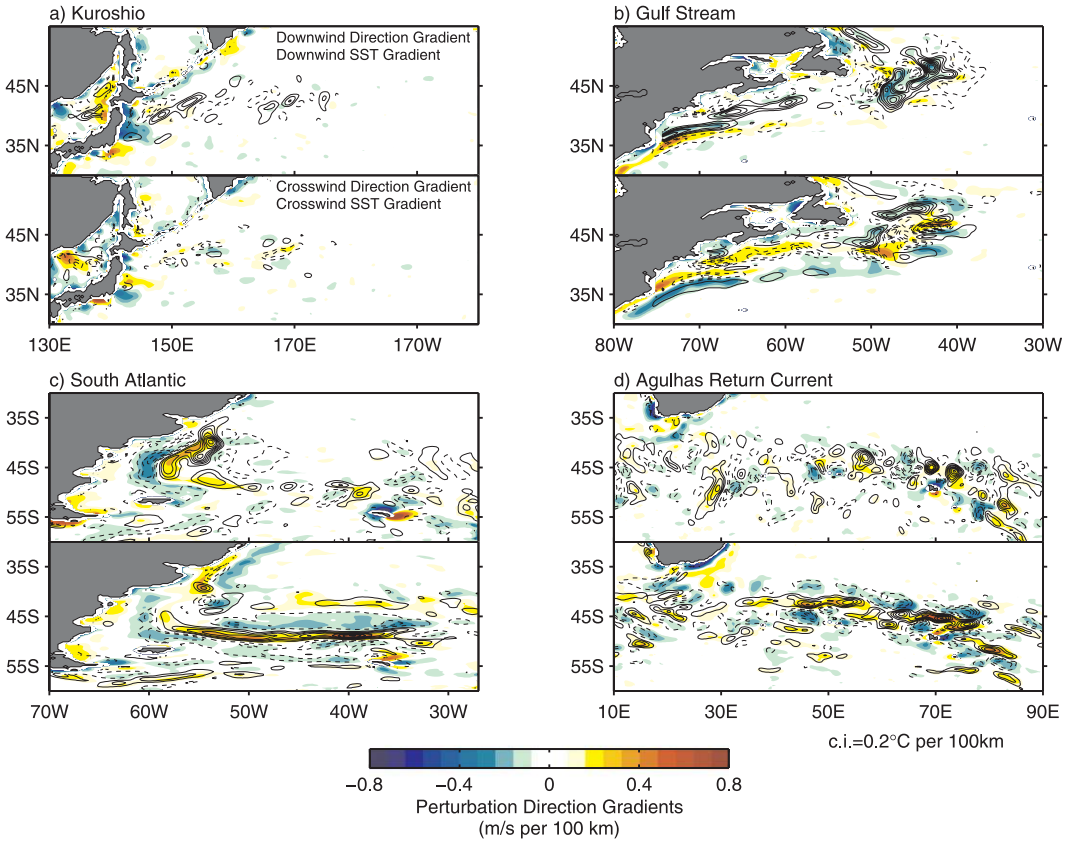

FIG. 13. (top maps in each panel) The perturbation crosswind direction gradient (colors) overlaid with contours of the crosswind SST gradient. (bottom maps in each panel) The perturbation downwind direction gradient (colors) overlaid with contours of the downwind SST gradient. The data in each map were averaged over the 75-month period June 2002–August 2008. The contour interval for the perturbation crosswind and downwind SST gradients is 0.2°C per 100 km, and the zero contour has been omitted for clarity. Solid and dashed contours correspond to positive and negative values of the SST gradient, respectively.

Acknowledgments. We thank Barry Vanhoff, Mike Freilich, and Michael Schlax for guidance in computing the in-swath derivative fields from the QuikSCAT measurement swaths used in this paper. We also thank Roger Samelson, Eric Skyllingstad, Justin Small, and Qingtao Song for helpful discussions throughout the course of this analysis, and two anonymous reviewers for their time and numerous comments that significantly improved the clarity of the results and discussion. The QuikSCAT raw swath data and gridded AMSR-E SST fields were obtained from Remote Sensing Systems, Santa Rosa, CA. AMSR-E data are sponsored by the NASA Earth Science MEaSUREs DISCOVER Project and the AMSR-E Science Team. QuikSCAT data are sponsored by the NASA Ocean Vector Winds Science Team. This research was supported by NASA Grant NAS5-32965 and Contract 1283973 from the NASA Jet Propulsion Laboratory for funding of Ocean Vector Winds Science Team activities. Part of this research was performed while the lead author held a National Research Council Research Associateship Award at the Naval Research Laboratory in Monterey, CA.

APPENDIX

Physical Interpretation of θ'

The angle θ' defined by Eq. (8) is important in quantifying the response of the surface perturbation vorticity and divergence fields to spatially varying SST. Nonlinearities and spatial high-pass filtering of the crosswind and downwind SST gradient fields make exact analytical formulation of θ' in terms of wind and SST intractable. Nevertheless, an effort is made here to clarify the practical physical relevance of θ' to the orientation of the surface winds to SST fronts, which conceptually control spatial gradients in wind speed and direction as discussed throughout this study.

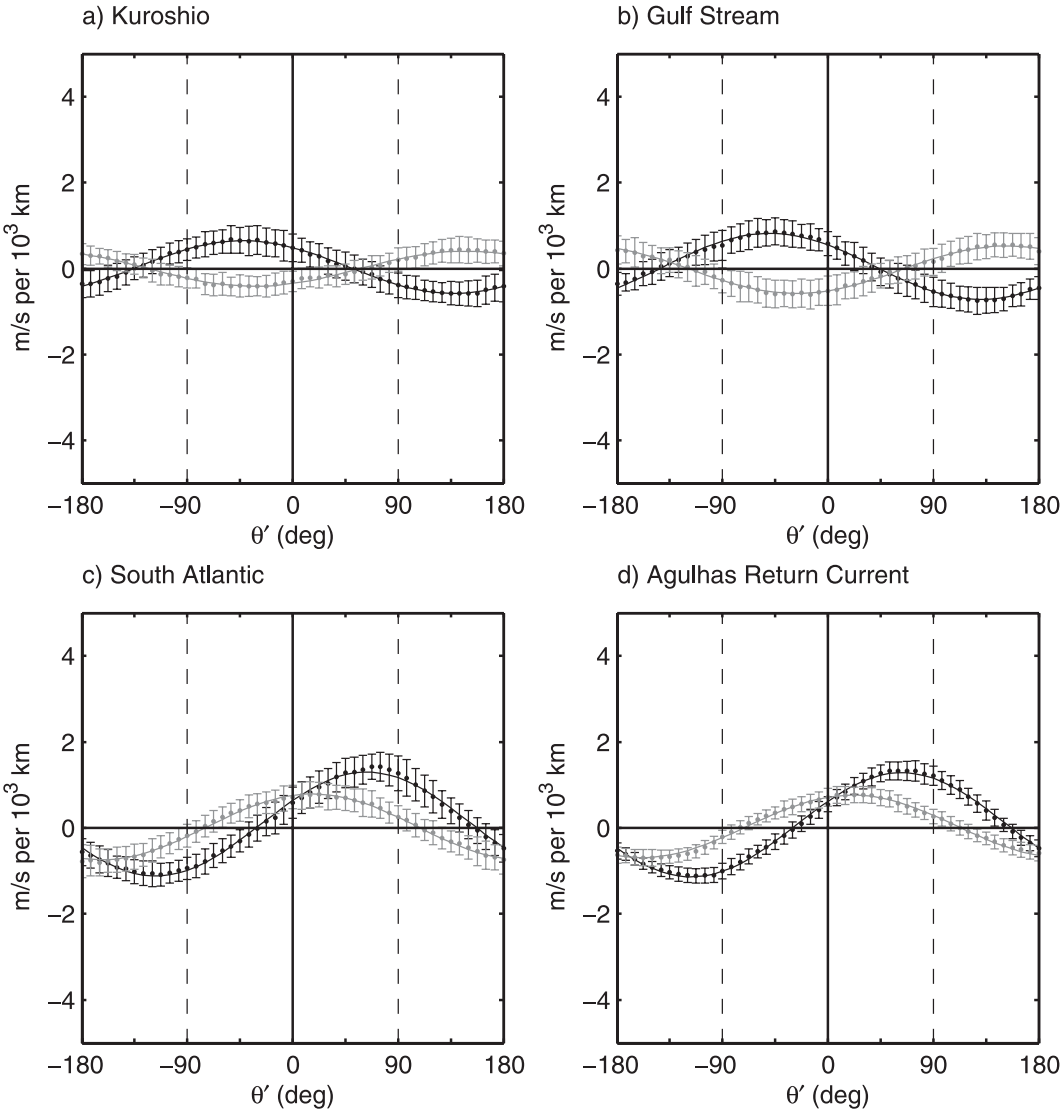

FIG. 14. As in Fig. 10, but for the perturbation crosswind (black) and downwind (gray) direction gradients as functions of θ'.

The unfiltered crosswind and downwind SST gradient components can be expanded as the sum of spatially high-pass filtered components, represented by primes, and smoothed, spatially low-pass filtered components, represented by tildes:

$$\frac{\partial T}{\partial n} = \left(\frac{\partial T}{\partial n}\right)' + \left(\frac{\widetilde{\partial T}}{\partial n}\right) \quad \text{and} \tag{A1}$$

$$\frac{\partial T}{\partial s} = \left(\frac{\partial T}{\partial s}\right)' + \left(\frac{\widetilde{\partial T}}{\partial s}\right). \tag{A2}$$

An empirical approximation can then be made by writing the crosswind and downwind SST gradient components in the following forms:

$$\left(\frac{\partial T}{\partial n}\right) = |\nabla T| \sin\theta, \tag{A3}$$

$$\left(\frac{\partial T}{\partial s}\right) = |\nabla T| \cos\theta, \tag{A4}$$

$$\left(\frac{\partial T}{\partial n}\right)' = |\nabla T'| \sin\theta', \tag{A5}$$

$$\left(\frac{\partial T}{\partial s}\right)' = |\nabla T'| \sin\theta', \tag{A6}$$

$$\left(\frac{\widetilde{\partial T}}{\partial n}\right) = |\nabla \widetilde{T}| \sin\tilde{\theta}, \quad \text{and} \tag{A7}$$

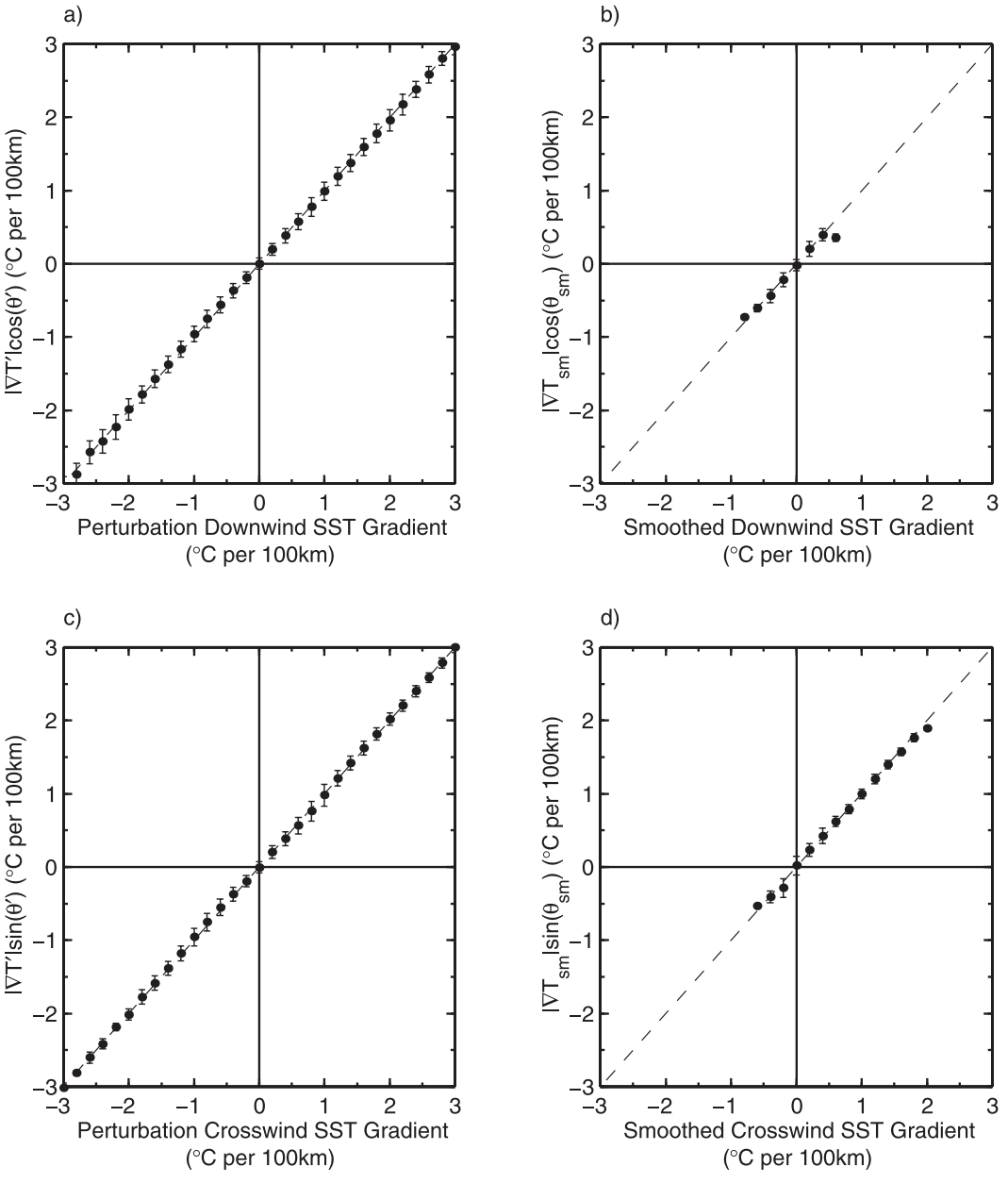

FIG. A1. Binned scatterplots of the relations expressed by Eqs. (A5)–(A8). (a) $|\nabla T'|\cos\theta'$ vs. $(\partial T/\partial s)'$; (b) $|\nabla \widetilde{T}|\cos\tilde{\theta}$ vs. $(\widetilde{\partial T/\partial s})$; (c) $|\nabla T'|\sin\tilde{\theta}$ vs. $(\widetilde{\partial T/\partial n})'$; (d) $|\nabla \tilde{T}|\sin\tilde{\theta}$ vs. $(\widetilde{\partial T/\partial n})$. The points and error bars in each panel represent the means and ±1 std dev within each bin computed from the first monthly averaged AMSR-E SST and QuikSCAT wind fields used in this study over the Agulhas Return Current. The dashed line in each panel has unit slope and is shown for reference.

$$\left(\frac{\widetilde{\partial T}}{\partial s}\right) = |\nabla \widetilde{T}|\cos\tilde{\theta}, \qquad \text{(A8)} \qquad \tilde{\theta} = \tan^{-1}\left[\frac{(\widetilde{\partial T/\partial n})}{(\widetilde{\partial T/\partial s})}\right].$$

where θ is defined as the counterclockwise angle between the surface wind vector and ∇T, θ' is defined as in Eq. (8), and $\tilde{\theta}$ is defined analogously as

Equations (A5)–(A8) are only approximations that cannot be rigorously justified analytically because the loess smoother used to produce the spatially filtered SST

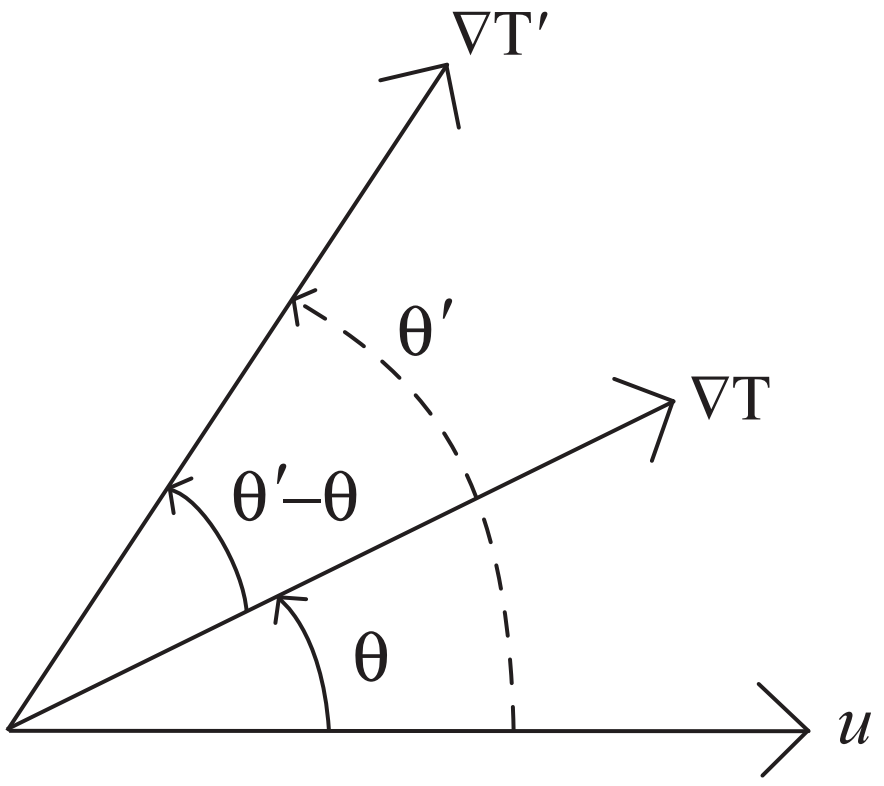

FIG. A2. Schematic of the orientation of the surface wind vector $\boldsymbol{u}$, the SST gradient vector ∇T, and the perturbation SST gradient vector $\nabla T'$. The counterclockwise angle $\theta' - \theta$ is as deduced from Eq. (A16).

fields here is not commutative with the nonlinear vector magnitude operator. However, they are shown empirically in Fig. A1 to be nearly exact, despite the nonlinearities, based on terms computed from the AMSR-E SST and QuikSCAT wind fields averaged over the 1-week period 29 December 2002–4 January 2003, which is representative of the 6+-year data record used here.

An interpretation of θ' can be obtained by eliminating $\tilde{\theta}$ and $\widetilde{T}$ from consideration and solving for θ' in terms of θ in a form that reveals that θ' is the angle between the wind vector $\mathbf{u}$ and the perturbation SST gradient vector $\nabla T'$. With the above forms, Eqs. (A1) and (A2) can be written as

$$|\nabla T| \sin\theta = |\nabla T'| \sin\theta' + |\nabla \widetilde{T}| \sin\tilde{\theta} \quad \text{and} \tag{A9}$$

$$|\nabla T| \cos\theta = |\nabla T'| \cos\theta' + |\nabla \widetilde{T}| \cos\tilde{\theta}. \tag{A10}$$

Squaring and adding these two equations yields

$$|\nabla T'|^2 + 2|\nabla T'||\nabla \widetilde{T}| \cos(\theta' - \tilde{\theta}) + |\nabla \widetilde{T}|^2 = |\nabla T|^2.$$

Hence,

$$\tilde{\theta} = \theta' - \cos^{-1} R, \tag{A11}$$

where

$$R = \frac{|\nabla T|^2 - |\nabla T'|^2 - |\nabla \widetilde{T}|^2}{2|\nabla T'||\nabla \widetilde{T}|}. \tag{A12}$$

Substituting Eq. (A11) into Eqs. (A9) and (A10) with the trigonometric identity $\sin(\cos^{-1} R) = \pm(1 - R^2)^{1/2}$ and summing sine and cosine trigonometric identities yields

$$|\nabla T| \sin\theta = |\nabla T'| \sin\theta' + |\nabla \widetilde{T}|[R \sin\theta' \pm (1 - R^2)^{1/2} \cos\theta'] \quad \text{and}$$

$$|\nabla T| \cos\theta = |\nabla T'| \cos\theta' + |\nabla \widetilde{T}|[R \cos\theta' \pm (1 - R^2)^{1/2} \sin\theta'].$$

These can be rewritten as

$$|\nabla T| \sin\theta = A \sin\theta' \pm B \cos\theta' \quad \text{and} \tag{A13}$$

$$|\nabla T| \cos\theta = A \cos\theta' \pm B \sin\theta', \tag{A14}$$

where $A = (|\nabla T'| + |\nabla \widetilde{T}| R)$ and $B = |\nabla \widetilde{T}|(1 - R^2)^{1/2}$. The positive or negative root in each equation means there are four possible sets of equations. However, by

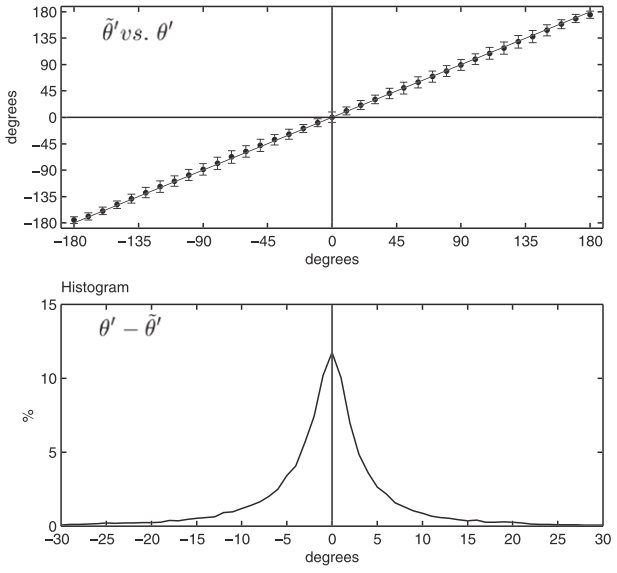

FIG. A3. (top) Binned scatterplot of the angle $\widehat{\theta'}$ between the surface wind vector and the perturbation SST gradient vector binned as a function of θ'. (bottom) Histogram of the differences between $\widehat{\theta'}$ and θ'; the distribution has a standard deviation of 7.6°. The points and error bars in the top panel represent the means and ±1 standard deviation within each bin computed from the first monthly-averaged AMSR-E SST and QuikSCAT wind fields used in this study over the Agulhas Return Current. The dashed line in the top panel has unit slope and is shown for reference.

noting that $A^2 + B^2 = |\nabla T|$, only two sets of equations are possible, namely

$$|\nabla T| \sin\theta = A \sin\theta' + B \cos\theta' \quad \text{and}$$

$$|\nabla T| \cos\theta = A \cos\theta' - B \sin\theta',$$

or

$$|\nabla T| \sin\theta = A \sin\theta' - B \cos\theta' \quad \text{and}$$

$$|\nabla T| \cos\theta = A \cos\theta' + B \sin\theta'.$$

A unique solution is obtained multiplying the first equation in each pair by $\sin\theta'$ and adding it to $\cos\theta'$ times the second equation. Doing so to both sets of equations gives the same result:

$$\cos(\theta - \theta') = \frac{A}{|\nabla T|} = \frac{|\nabla T|^2 + |\nabla T'|^2 - |\nabla \widetilde{T}|^2}{2|\nabla T||\nabla T'|}. \tag{A15}$$

This equation can be simplified by substituting $\widetilde{T} = T - T'$ to eliminate the low-pass filtered SST field from consideration and expanding the gradient terms into component form:

$$|\nabla T|^2 = \left(\frac{\partial T}{\partial x}\right)^2 + \left(\frac{\partial T}{\partial y}\right)^2,$$

$$|\nabla T'|^2 = \left(\frac{\partial T'}{\partial x}\right)^2 + \left(\frac{\partial T'}{\partial y}\right)^2, \quad \text{and}$$

$$|\nabla \widetilde{T}|^2 = \left(\frac{\partial T}{\partial x} - \frac{\partial T'}{\partial x}\right)^2 + \left(\frac{\partial T}{\partial y} - \frac{\partial T'}{\partial y}\right)^2.$$

Using these relations, and after some manipulation and simplification, Eq. (A15) can be written in the compact form

$$\cos(\theta' - \theta) = \frac{\nabla T \cdot \nabla T'}{|\nabla T||\nabla T'|}. \tag{A16}$$

From the definition of the dot product in the numerator of Eq. (A16), it is evident that the angle $\theta' - \theta$ is the counterclockwise angle between the vectors ∇T and $\nabla T'$. A schematic of these angles and SST gradient vectors is shown in Fig. A2. From this, it can be deduced that θ' is the counterclockwise angle between **u** and the perturbation SST gradient vector $\nabla T'$. This deduction is confirmed statistically in the top panel of Fig. A3, where the angle between **u** and $\nabla T'$, denoted as $\hat{\theta}'$, is binned as a function of the angle θ' computed from Eq. (8) using the 6+ years of monthly-averaged QuikSCAT wind and AMSR-E SST fields utilized in this study. Differences are quantified in the histogram in the bottom panel of Fig. A3, which shows a very narrow distribution centered at 0° with a standard deviation of 7.6°. It is thus concluded that the angle between the surface wind and perturbation SST gradient vectors is very well represented by the angle θ'.

REFERENCES

Battisti, D. S., E. S. Sarachik, and A. C. Hirst, 1999: A consistent model for the large-scale steady surface atmospheric circulation in the tropics. *J. Climate,* **12,** 2956–2964.

Bond, N. A., 1992: Observations of planetary boundary-layer structure in the eastern equatorial Pacific. *J. Climate,* **5,** 699–706.

Bourras, D., G. Reverdin, H. Giordani, and G. Caniaux, 2004: Response of the atmospheric boundary layer to a mesoscale oceanic eddy in the northeast Atlantic. *J. Geophys. Res.,* **109,** D18114, doi:10.1029/2004JD004799.

Cayan, D. R., 1992: Latent and sensible heat flux anomalies over the northern oceans: Driving the sea surface temperature. *J. Phys. Oceanogr.,* **22,** 859–881.

Chelton, D. B., 2005: The impact of SST specification on ECMWF surface wind stress fields in the eastern tropical Pacific. *J. Climate,* **18,** 530–550.

——, and M. G. Schlax, 2003: The accuracies of smoothed sea surface height fields constructed from tandem altimeter datasets. *J. Atmos. Oceanic Technol.,* **20,** 1276–1302.

——, and M. H. Freilich, 2005: Scatterometer-based assessment of 10-m wind analyses from the operational ECMWF and NCEP

numerical weather prediction models. *Mon. Wea. Rev.,* **133,** 409–429.

——, and F. J. Wentz, 2005: Global microwave satellite observations of sea surface temperature for numerical weather prediction and climate research. *Bull. Amer. Meteor. Soc.,* **86,** 1097–1115.

——, and Coauthors, 2001: Observations of coupling between surface wind stress and sea surface temperature in the eastern tropical Pacific. *J. Climate,* **14,** 1479–1498.

——, M. G. Schlax, M. H. Freilich, and R. F. Milliff, 2004: Satellite measurements reveal persistent small-scale features in ocean winds. *Science,* **303,** 978–983.

——, ——, and R. M. Samelson, 2007: Summertime coupling between sea surface temperature and wind stress in the California Current System. *J. Phys. Oceanogr.,* **37,** 495–517.

Cleveland, W. S., and S. J. Devlin, 1988: Locally weighted regression: An approach to regression analysis by local fitting. *J. Amer. Stat. Assoc.,* **83,** 596–610.

Cronin, M. F., S.-P. Xie, and H. Hashizume, 2003: Barometric pressure variations associated with eastern Pacific tropical instability waves. *J. Climate,* **16,** 3050–3057.

de Szoeke, S. P., and C. S. Bretherton, 2004: Quasi-Lagrangian large eddy simulations of cross-equatorial flow in the east Pacific atmospheric boundary layer. *J. Atmos. Sci.,* **61,** 1837–1858.

——, ——, N. A. Bond, M. F. Cronin, and B. M. Morley, 2005: EPIC 95°W observations of the eastern Pacific atmosphere boundary layer from the cold tongue to the ITCZ. *J. Atmos. Sci.,* **62,** 426–442.

Ebuchi, N., H. C. Graber, and M. J. Caruso, 2002: Evaluation of wind vectors observed by QuikSCAT/SeaWinds using ocean buoy data. *J. Atmos. Oceanic Technol.,* **19,** 2049–2062.

Freihe, C. A., and Coauthors, 1991: Air–sea fluxes and surface layer turbulence around a sea surface temperature front. *J. Geophys. Res.,* **96,** 8593–8609.

Haack, T., D. Chelton, J. Pullen, J. D. Doyle, and M. Schlax, 2008: Summertime influence of SST on surface wind stress off the U.S. west coast from the U.S. Navy COAMPS model. *J. Phys. Oceanogr.,* **38,** 2414–2437.

Haltiner, G. J., and F. L. Martin, 1957: *Dynamical and Physical Meteorology*. McGraw-Hill, 470 pp.

Hashizume, H., S.-P. Xie, M. Fujiwara, M. Shiotani, T. Watanabe, Y. Tanimoto, W. T. Liu, and K. Takeuchi, 2002: Direct observations of atmospheric boundary layer response to SST variations associated with tropical instability waves over the eastern equatorial Pacific. *J. Climate,* **15,** 3379–3393.

Hayes, S. P., M. J. McPhaden, and J. M. Wallace, 1989: The influence of sea-surface temperature on surface wind in the eastern equatorial Pacific. *J. Climate,* **2,** 1500–1506.

Hogg, A. C. M., W. K. Dewar, P. Berloff, S. Kravtsov, and D. K. Hutchinson, 2009: The effects of mesoscale ocean–atmosphere coupling on the large-scale ocean circulation. *J. Climate,* **22,** 4066–4082.

Holton, J. R., 1992: *An Introduction to Dynamic Meteorology*. 1st ed. Academic Press, 511 pp.

Jin, X., C. Dong, J. Kurian, J. C. McWilliams, D. B. Chelton, and Z. Li, 2009: SST–wind interaction in coastal upwelling: Oceanic simulation with empirical coupling. *J. Phys. Oceanogr.,* **39,** 2957–2970.

Jury, M. R., 1994: Thermal front within the marine atmospheric boundary layer over the Agulhas Current south of Africa: Composite aircraft observations. *J. Geophys. Res.,* **99,** 3297–3304.

Lindzen, R. S., and S. Nigam, 1987: On the role of sea surface temperature gradients in forcing low-level winds and convergence in the tropics. *J. Atmos. Sci.,* **44,** 2418–2436.

Liu, W. T., and W. Tang, 1996: Equivalent neutral wind. JPL Publication 96–17, 8 pp.

——, X. Xie, and P. Niiler, 2007: Ocean–atmosphere interaction over Agulhas Extension meanders. *J. Climate,* **20,** 5784–5797.

Mahrt, L., D. Vickers, and E. Moore, 2004: Flow adjustments across sea-surface temperature changes. *Bound.-Layer Meteor.,* **111,** 553–564.

Maloney, E. D., and D. B. Chelton, 2006: An assessment of the sea surface temperature influence on surface wind stress in numerical weather prediction and climate models. *J. Climate,* **19,** 2743–2762.

Mantua, N. J., S. R. Hare, Y. Zhang, J. M. Wallace, and R. C. Francis, 1997: A Pacific interdecadal climate oscillation with impacts on salmon production. *Bull. Amer. Meteor. Soc.,* **78,** 1069–1079.

Mears, C. A., D. K. Smith, and F. J. Wentz, 2001: Comparison of Special Sensor Microwave Imager and buoy-measured wind speeds from 1987 to 1997. *J. Geophys. Res.,* **106,** 11 719–11 729.

Mey, R. D., and N. D. Walker, 1990: Surface heat fluxes and marine boundary layer modification in the Agulhas Retroflection region. *J. Geophys. Res.,* **95,** 15 997–16 015.

Milliff, R. F., W. G. Large, W. R. Holland, and J. C. McWilliams, 1996: The general circulation responses of high-resolution North Atlantic Ocean models to synthetic scatterometer winds. *J. Phys. Oceanogr.,* **26,** 1747–1768.

Nonaka, M., and S.-P. Xie, 2003: Covariations of sea surface temperature and wind over the Kuroshio and its extension: Evidence for ocean-to-atmosphere feedback. *J. Climate,* **16,** 1404–1413.

Norris, J. R., and S. F. Iacobellis, 2005: North Pacific cloud feedbacks inferred from synoptic-scale dynamic and thermodynamic relationships. *J. Climate,* **18,** 4862–4878.

Okumura, Y., S.-P. Xie, A. Numaguti, and Y. Tanimoto, 2001: Tropical Atlantic air–sea interaction and its influence on the NAO. *Geophys. Res. Lett.,* **28,** 1507–1510.

O'Neill, L. W., D. B. Chelton, and S. K. Esbensen, 2003: Observations of SST-induced perturbations on the wind stress field over the Southern Ocean on seasonal time scales. *J. Climate,* **16,** 2340–2354.

——, ——, ——, and F. J. Wentz, 2005: High-resolution satellite measurements of the atmospheric boundary layer response to SST perturbations over the Agulhas Return Current. *J. Climate,* **18,** 2706–2723.

——, S. K. Esbensen, N. Thum, R. M. Samelson, and D. B. Chelton, 2010: Dynamical analysis of the boundary layer and surface wind responses to mesoscale SST perturbations. *J. Climate,* in press.

Park, K.-A., and P. C. Cornillon, 2002: Stability-induced modification of sea surface winds over Gulf Stream rings. *Geophys. Res. Lett.,* **29,** 2211, doi:10.1029/2001GL014236.

——, ——, and D. L. Codiga, 2006: Modification of surface winds near ocean fronts: Effects of Gulf Stream rings on scatterometer (QuikSCAT, NSCAT) wind observations. *J. Geophys. Res.,* **111,** C03021, doi:10.1029/2005JC003016.

Rouault, M., and J. R. E. Lutjeharms, 2000: Air–sea exchange over an Agulhas eddy at the subtropical convergence. *Global Atmos. Ocean Syst.,* **7,** 125–150.

Samelson, R. M., E. D. Skyllingstad, D. B. Chelton, S. K. Esbensen, L. W. O'Neill, and N. Thum, 2006: On the coupling of wind stress and sea surface temperature. *J. Climate,* **19,** 1557–1566.

Schlax, M. G., D. B. Chelton, and M. H. Freilich, 2001: Sampling errors in wind fields constructed from single and tandem scatterometer datasets. *J. Atmos. Oceanic Technol.,* **18,** 1014–1036.

Seo, H., A. J. Miller, and J. O. Roads, 2007: The Scripps coupled ocean–atmosphere regional (SCOAR) model, with applications in the eastern Pacific sector. *J. Climate,* **20,** 381–402.

Skyllingstad, E. D., D. Vickers, L. Mahrt, and R. Samelson, 2006: Effects of mesoscale sea-surface temperature fronts on the marine atmospheric boundary layer. *Bound.-Layer Meteor.,* **123,** 219–237, doi:10.1007/s10546-006-9127-8.

Small, R. J., S.-P. Xie, and Y. Wang, 2003: Numerical simulation of atmospheric response to Pacific tropical instability waves. *J. Climate,* **16,** 3723–3741.

——, ——, and J. Hafner, 2005a: Satellite observations of mesoscale ocean features and copropagating atmospheric surface fields in the tropical belt. *J. Geophys. Res.,* **110,** C02021, doi:10.1029/2004JC002598.

——, ——, Y. Wang, S. K. Esbensen, and D. Vickers, 2005b: Numerical simulation of boundary layer structure and cross-equatorial flow in the eastern Pacific. *J. Atmos. Sci.,* **62,** 1812–1830.

——, and Coauthors, 2008: Air–sea interaction over ocean fronts and eddies. *Dyn. Atmos. Oceans,* **45,** 274–319, doi:10.1016/j.dynatmoce.2008.01.001.

——, K. J. Richards, S.-P. Xie, P. Dutrieux, and T. Miyama, 2009: Damping of tropical instability waves caused by the action of surface currents on stress. *J. Geophys. Res.,* **114,** C04009, doi:10.1029/2008JC005147.

Song, Q., T. Hara, P. Cornillon, and C. A. Friehe, 2004: A comparison between observations and MM5 simulations of the marine atmospheric boundary layer across a temperature front. *J. Atmos. Oceanic Technol.,* **21,** 170–178.

——, P. Cornillon, and T. Hara, 2006: Surface wind response to oceanic fronts. *J. Geophys. Res.,* **111,** C12006, doi:10.1029/2006JC003680.

——, D. B. Chelton, S. K. Esbensen, N. Thum, and L. W. O'Neill, 2009: Coupling between sea surface temperature and low-level winds in mesoscale numerical models. *J. Climate,* **22,** 146–164.

Spall, M. A., 2007a: Effect of sea surface temperature–wind stress coupling on baroclinic instability in the ocean. *J. Phys. Oceanogr.,* **37,** 1092–1097.

——, 2007b: Midlatitude wind stress–sea surface temperature coupling in the vicinity of oceanic fronts. *J. Climate,* **20,** 3785–3801.

Stevens, B., J. Duan, J. C. McWilliams, M. Münnich, and J. D. Neelin, 2002: Entrainment, Rayleigh friction, and boundary layer winds over the tropical Pacific. *J. Climate,* **15,** 30–44.

Sweet, W. R., R. Fett, J. Kerling, and P. LaViolette, 1981: Air–sea interaction effects in the lower troposphere across the north wall of the Gulf Stream. *Mon. Wea. Rev.,* **109,** 1042–1052.

Thum, N., 2006: Atmospheric boundary layer coupling to midlatitude mesoscale sea surface temperature anomalies. Ph.D. thesis, Oregon State University, 142 pp. [Available from University Microfilm, 305 N. Zeeb Rd., Ann Arbor, MI 48106.]

Tokinaga, H., and Coauthors, 2006: Atmospheric sounding over the winter Kuroshio Extension: Effect of surface stability on atmospheric boundary layer structure. *Geophys. Res. Lett.,* **33,** L04703, doi:10.1029/2005GL025102.

Wai, M., and S. A. Stage, 1989: Dynamical analysis of marine atmospheric boundary layer structure near the Gulf Stream oceanic front. *Quart. J. Roy. Meteor. Soc.,* **115,** 29–44.

Wallace, J. M., T. P. Mitchell, and C. Deser, 1989: The influence of sea surface temperature on surface wind in the eastern equatorial Pacific: Seasonal and interannual variability. *J. Climate,* **2,** 1492–1499.

Warner, T. T., M. N. Lakhtakia, J. D. Doyle, and R. A. Pearson, 1990: Marine atmospheric boundary layer circulations forced by Gulf Stream sea surface temperature gradients. *Mon. Wea. Rev.,* **118,** 309–323.

Wentz, F. J., and T. Meissner, 2000: AMSR Ocean Algorithm, version 2. Tech. Rep. 121599A–1, Remote Sensing Systems, 66 pp.

White, W. B., and J. L. Annis, 2003: Coupling of extratropical mesoscale eddies in the ocean to westerly winds in the atmospheric boundary layer. *J. Climate,* **33,** 1095–1107.

Xie, S.-P., 2004: Satellite observations of cool ocean–atmosphere interaction. *Bull. Amer. Meteor. Soc.,* **85,** 195–208.